**Supplemental Information**

**for**

# Bacterial swarming reduces *Proteus mirabilis* and *Vibrio parahaemolyticus* cell stiffness and increases β-lactam susceptibility

George K. Auer[a], Piercen M. Oliver[b], Manohary Rajendram[b], Qing Yao[c,d], Grant J. Jensen[c, d], and Douglas B. Weibel[a,b,e*]

[a] Department of Biomedical Engineering, University of Wisconsin-Madison, Madison, WI, 53706
[b] Department of Biochemistry, University of Wisconsin-Madison, Madison, WI, 53706
[c] Division of Biology and Biological Engineering, California Institute of Technology, Pasadena, CA 91125
[d] Howard Hughes Medical Institute, California Institute of Technology, Pasadena, CA 91125
[e] Department of Chemistry, University of Wisconsin-Madison, Madison, WI, 53706

*** Author to whom correspondence should be addressed:**
Douglas B. Weibel
Department of Biochemistry
6424 Biochemical Sciences Building
440 Henry Mall
Phone: +1 (608) 890-1342
Fax: +1 (608) 265-0764
E-mail: douglas.weibel@wisc.edu

## 1. METHODS

**Immunostaining flagella on *E. coli* cells to determine flagella surface density.** As a control to determine the influence of the surface density of bacterial flagella on measurements of bending rigidity, we imaged two *E. coli* MG1655 strains with different flagella densities using a polyclonal flagellin antibody and an immunostaining procedure for flagella visualization (1).

**Calculating vegetative and swarmer cell division times.** We prepared vegetative cells by diluting an overnight culture 1:200 in fresh medium and grew the cells at 30 °C with shaking at 200 rpm to an optical density (OD; λ=600 nm) of 0.6. We prepared swarmer cells as described previously (1). We monitored the growth of *P. mirabilis*, *V. parahaemolyticus*, and *E. coli* vegetative cells over 120 min at 30 °C in the microfluidic flow chamber device described in the next section. We performed a similar experiment with *P. mirabilis* and *V. parahaemolyticus* swarmers growing over 65 min at 30 °C to determine the amount of time elapsed before cells divided. We collected images of cells at 1-min intervals and determined the division time for a maximum of 10 generations (for vegetative cells) and 4 division events (for swarmer cells).

**Measuring the sensitivity of cells to osmotic shock in a microfluidic device.** We prepared filamentous vegetative cells of *P. mirabilis* and *V. parahaemolyticus* by diluting

52 an overnight culture of cells 1:200 into fresh medium. We then grew cultures at 30 °C
53 with shaking for 1 h, added aztreonam (MP Biomedicals) to a final concentration of 10
54 μg/mL and grew cells for an additional 70 min. Swarmer cells were prepared as
55 described previously (1). To maximize the number of cells attached to a surface in the
56 microfluidic device (flow chamber construction described below), we concentrated cells
57 to an $OD_{600}$ of 8 in 100 μL of liquid nutrient medium.

58 We prepared the microfluidic device for experiments by flowing 10 μL of
59 undiluted Cell-Tak (Corning) into the device and incubated it for 10 min at 25 °C. Next,
60 we flowed 20 μL of a suspension of cells ($OD_{600}$=8) through the device, then repeated
61 with another 20 μL aliquot of cell suspension. To aid the adherence of the highly motile
62 swarmer cells to the Cell-Tak-coated surface, we centrifuged the device for 5 min at 300
63 x *g* in a centrifuge (Beckman Coulter) equipped with a swinging bucket rotor.

64 For osmotic shock experiments, we filled separate 1-mL syringes (BD) with a
65 solution of UltraPure distilled water (Invitrogen) or 1 M of a NaCl solution prepared in
66 dd$H_2O$ and connected the syringes using a three-way valve. We mounted the
67 microfluidic device on a TE2000-E inverted microscope and imaged cells in the chamber
68 at 25 °C (decreasing the temperature reduced growth and cell division). Prior to osmotic
69 shock, we flowed 200 μL of fresh liquid media (PLB for *P. mirabilis*, LB for *E. coli*, and HI
70 for *V. parahaemolyticus*) through the device to remove cells that were not adhered to the
71 channel surface. While imaging, we flowed a 1 M NaCl solution through the channel

and observed cell plasmolysis, immediately after which we flowed $ddH_2O$ through the channel and observed cells elongating. We collected images of hundreds of single cells after exposing them to three conditions: 1) isotonic culture (PLB, LB, HI); 2) hypertonic shock (1 M NaCl); and 3) hypotonic shock ($ddH_2O$).

To determine changes in cell size and width, we extracted individual cell contours from the images taken for each treatment using MATLAB 2014a (MathWorks) and used MicrobeTracker (2) to determine cell lengths ($L$) and widths ($W$). From these measurements we calculated $\Delta L$ ($L_{\text{hypotonic}} - L_{\text{hypertonic}}$) and $\Delta W$ ($W_{\text{hypotonic}} - W_{\text{hypertonic}}$) for vegetative and swarmer cells of *P. mirabilis* and *V. parahaemolyticus*.

**Determining the minimum inhibitory concentration (MIC) of vegetative cells of *P. mirabilis* and *V. parahaemolyticus*.** We used the micro-dilution protocol (3) to determine the MIC of cephalexin in accordance with Clinical and Laboratory Standards Institute. Briefly, we added 400 μg/mL of cephalexin (BP Biomedicals) or penicillin G (BP Biomedicals) to the first well of a 96-well microplate (Nunc) and diluted these antibiotics 2-fold across adjacent wells (wells #1-11); well 12 was a no-drug control. We determined the MIC after 16 h of growth at 30 °C with shaking by identifying the lowest concentration of cephalexin and penicillin G that inhibited cell growth by visual inspection. The MIC was determined from three replicate plates. We determined the MIC of cephalexin against *E. coli* MG1655 (1X MIC = 6.25 μg/mL, 32X

MIC = 200 μg/mL), *P. mirabilis* (100 μg/mL), and *V. parahaemolyticus* (50 μg/mL). The MIC of penicillin G against *P. mirabilis* was 12.5 μg/mL.

**Antibiotic treatment of vegetative and swarmer cells and measurement of their growth in a microfluidic device.** We prepared vegetative and swarmer cells of *P. mirabilis* and *V. parahaemolyticus* as described above. Prior to use, we diluted cells 1:100 in fresh medium to a cell density that enabled us to image many individual cells simultaneously in the microfluidic device described in the section above.

To prepare the microfluidic device for monitoring growth, we applied a 250 μm-thick layer of PDMS prepolymer to the surface of (#1.5, 35 x 50 mm) cover glass (FisherBrand) using a spincoater (Laurell Technologies) and polymerized the polymer overnight at 60 °C. We subsequently removed a 6 mm x 4 mm rectangle of PDMS from the center of the cover glass using a scalpel. We applied transparent tape to both sides of this rectangular well and pipetted 100 μL of media containing a 2% (w/v) solution UltraPure agarose (Invitrogen) into the well. We placed a (#1.5, 22 x 30 mm) cover glass (FisherBrand) on top of the liquid agarose (to flatten the agarose surface), pressed the cover glass against the transparent tape, and solidified the agarose at 25 °C. Next, we removed the #1.5 cover glass, tape, and any residual agarose from the PDMS surface. We pipetted 2 μL of a suspension of cells on the agarose pad surface, waited until the excess liquid had evaporated or been absorbed by the agarose, carefully removed the

agarose layer, inverted it, and placed it back into the well such that the cells were positioned between the agarose surface and the cover glass. We placed the PDMS flow chamber used in the construction of the osmotic shock microfluidic device on the PDMS-coated cover glass and aligned it such that the agarose pad was centered in the flow channel (Fig. S11).

For antibiotic treatment of cells in the microfluidic cell growth device, we filled a 6-mL syringe (Norm-Ject) with cephalexin or penicillin G at a concentration corresponding to 1X MIC dissolved in nutrient medium. We supplied a constant flow of 20 μL/min to the device using a syringe pump (Harvard Apparatus) and monitored the growth of individual cells during antibiotic exposure using a TE2000-E inverted microscope. The stage and objective heater were maintained at 30 °C. Images were collected every 1 min for 3 h.

Due to the aberrant shape of cells treated with cephalexin and penicillin G (Fig. S12), we were unable to use an automated script (e.g., MicrobeTracker) to determine cell death. Instead, we visually determined the time of death for individual cells when they exhibited three phenotypes that collectively indicate cell death: blebbing (membrane swelling), lysis (bleb rupture), and disappearance of cells in phase contrast microscopy (loss of cytoplasmic material).

**Determining cell growth rates in the presence of antibiotics.** We prepared vegetative and swarmer cells of *P. mirabilis* and *V. parahaemolyticus* as described above. We monitored individual cell growth at 30 °C in the presence of 1X MIC of cephalexin and pencillin G in our microfluidic growth device (described above) by collecting an image every 1 min for 15 min. To calculate the growth rate, we first extracted individual cell contours at each time point using MicrobeTracker and determined cell length. To take into account the differences in starting length between *P. mirabilis* and *V. parahaemolyticus* cells, we normalized the change in length to the initial cell length ($\Delta L/L_0$) at each time point. To determine the growth rate for individual cells, we fit their relative length over time to an exponential function using GraphPad Prism 6.0 (GraphPad Software).

**Measuring cell envelope architecture and peptidoglycan thickness using electron cryotomography.** We prepared vegetative and swarmer cells of *P. mirabilis* and *V. parahaemolyticus* and concentrated them to an $OD_{600}$=10. For ECT, we mixed vegetative and swarmer cells with bovine serum albumin-treated 10-nm diameter gold particles that served as fiducial markers, applied them to electron microscopy grids, and plunge-froze them in a mixture of liquid ethane and propane, as described previously (4). Grids were stored in liquid nitrogen until imaging.

We acquired images on a 300 KeV Polara transmission electron microscope (FEI) with a GIF energy filter (Gatan) and a K2 Summit direct detector (Gatan). We collected tilt series from -60° to +60° with 1° increments using UCSFtomo software with a defocus of -10 μm and a total dosage of 190 $e^-/Å^2$ (5) at a magnification of 27500×. Tomograms were calculated using IMOD software (6).

For sub-tomogram averaging, smooth and flat membrane regions were chosen by eye; a volume of 40 × 70 × 12 voxels (62 nm × 109 nm × 19 nm) was centered using the outer membrane and extracted. We aligned 38 extracted "membrane fragments" from four *P. mirabilis* vegetative cells and 42 fragments from nine *P. mirabilis* swarmer cells and averaged them in PEET (7). The densities from two averaged membranes were scaled to match each other using IMOD (6), cross-averaged density profiles were measured using ImageJ 1.50c (8), and figures were generated in OriginPro (OriginLab).

**Determining the thickness of *P. mirabilis* and *V. parahaemolyticus* sacculi (isolated peptidoglycan) by atomic force microscopy (AFM) in ambient conditions.** We isolated *P. mirabilis* and *V. parahaemolyticus* swarmer cells, concentrated them at 800 x *g* for 10 min, removed the supernatant, flash froze the cell pellet in liquid nitrogen, and stored it at -80 °C. Swarmer cell pellets were thawed at 4 °C and pooled for isolation of sacculi (intact peptidoglycan). To increase the efficiency of cell lysis prior to isolating sacculi, we resuspended vegetative and swarmer cell pellets in 3 mL of cold 1X phosphate-

buffered saline (ThermoScientific), then lysed cells with a tip sonicator (Qsonica) for ~10 s at a power setting of 75%. We confirmed cell lysis using optical microscopy. We isolated sonicated cells, resuspended sacculi in 20 (*V. parahaemolyticus* swarmers) or 200 μL of dd$H_2O$ (all other cells), immediately flash froze the sacculi in liquid nitrogen, and stored them at -80 °C**.**

To prepare sacculi for AFM, we transferred 10 μL of sacculi thawed at 4 °C to a new microcentrifuge tube placed in a bath sonicator (Branson) that was cooled with ice for 10 min to aid in the dispersal of sacculi without affecting sacculus architecture (9). After sonication, we pipetted 10 μL of the sacculi onto freshly cleaved mica (Ted Pella), dried the mica under nitrogen gas, washed it 3x with 1 mL of dd$H_2O$ (filtered through a 0.2 μm-diameter pore filter (Corning)), dried the sacculi under nitrogen gas, and imaged immediately after preparation.

We performed AFM using a Catalyst AFM (Bruker) operating in tapping mode in ambient conditions (air) with an aluminum reflex-coated silicon AFM probe (Ted Pella; k = 40 N/m). Before imaging, AFM probes were auto-tuned using Nanoscope 8.15 (Bruker). We collected all images at high resolution (512 x 512 pixels) with a scan speed of 1 Hz and analyzed images using NanoScope Analysis 1.4 (Bruker). Prior to determining sacculi thickness, we flattened ($0^{th}$ order) all images to remove variations in surface thickness. Thickness was determined perpendicular to the long axis; we avoided surface debris, folds in the sacculi, and trapped material in sacculi (Fig. S7).

**Determining the composition of peptidoglycan in *P. mirabilis* and *V. parahaemolyticus* vegetative and swarmer cells using ultra high performance liquid chromatography/mass spectrometry (UPLC/MS).** We prepared vegetative and swarmer cells of *P. mirabilis* and *V. parahaemolyticus* as described above. To purify peptidoglycan for UPLC/MS, we carried out a previously reported isolation technique for Gram-negative bacteria (10) with the following modifications. Briefly, after trypsin (Sigma) inactivation, we incubated the sacculi in 1 M HCl solution (Fluka) for 4 h at 37 °C to remove any O-acetylation from the peptidoglycan, which is present in *P. mirabilis* (11). Then, the sacculi were washed three times in dd$H_2O$, resuspended in 500 mM boric acid (Sigma) [pH 9] to $OD_{600}$=3, and mixed with 1/10 the volume of mutanolysin (Sigma). The sample was incubated 16 h at 37 °C with 200 rpm shaking. The next day, the samples were centrifuged for 10 min at 9500 x *g*, pelleting the remaining insoluble material. The supernatant was removed and put into a glass vial. To reduce the isolated muropeptide fragments, we added 50 μL of 20 μg/mL sodium borohydride (Sigma) in 500 mM boric acid [pH 9] and incubated the mixture for 30 min at 25 °C. We adjusted the pH of the solution to 2-3 by adding 50% phosphoric acid (Fluka), then filtered the muropeptide solution through a Duropore polyvinylidine fluoride filter (0.22-μm pores; Millex) into a clean vial. Vials were immediately stored at -80 °C until use within 1 week of muropeptide isolation.

For UPLC/MS, we injected 7.5 μL of purified muropeptides on a Cortecs 2.1 x 100 mm C18 column (Waters) packed with 1.6 μM-diameter particles and equipped with a Cortecs C18 guard column (Waters). The column temperature was maintained at 52 °C using an Acquity standard flow UPLC system equipped with an inline photodiode array (Waters). For muropeptide separation by UPLC, we used solvent A (Optima LCMS-grade water with 0.05% trifluoroacetic acid) and solvent B (30% (v/v) Optima LCMS-grade methanol in Optima LCMS-grade water with 0.05% trifluoroacetic acid) (Fisher Scientific). Muropeptides were eluted from the column with a gradient of increasing solvent B (1 min hold at 1% B, ramp to 99% B over 59 min, hold at 99% B for 5 min, then decrease to 1% B over 1.5 min, then hold at 1% B for 4.5 min) at a flow rate of 0.2 mL/min. We analyzed the eluent from the column using a Bruker MaXis Ultra-High Resolution time-of-flight 4G mass spectrometer (Bruker Daltonic) with either an MS method or a data-dependent, top 3 MS/MS method. For both methods, capillary voltage was set to 4100 V, the nebulizer pressure was 2.0 bar, and the drying gas was set to 6.0 L/m at 220 °C. Muropeptides were detected at λ=205 nm by MS.

We determined the peptidoglycan composition of *E. coli*, *P. mirabilis*, and *V. parahaemolyticus* vegetative and swarmer cells by comparing MS/MS fragmentation patterns using DataAnalysis version 4.2 (Bruker) (Fig. S*6*). Muropeptides were identified according to mass values using DataAnalysis 4.2. We calculated muropeptide masses using ChemDraw 14.0 (CambridgeSoft) (Table S1). We quantified the

corresponding UV (λ=205) absorbing peaks (Fig. S5) identified by MS (Bruker) from which we calculated peptidoglycan cross-linking density and strand length (12) for each species. Statistical significance was determined using GraphPad Prism 6.0

**Fabrication of microfluidic devices for measuring cell bending and cell growth.** Masters for the cell bending device and the cell growth/osmotic shock device were fabricated on separate 3" silicon wafers using SU8 photoresist that was exposed on a Heidelberg μPG101 mask writer (Heidelberg Instruments, Heidelberg, Germany) and developed. The bending device (Fig. S1) is a 2-layer device. The first SU8 layer consists of ~1 μm tall channels for capturing cells. The wafer was then coated with the second SU8 layer (~25 μm tall) that formed a central flow channel. The flow chamber (Fig. S11), consists of a single channel with a length of 10 mm, a width of 5 mm, and a height of 50 μm. The volume of the flow chamber is ~10 μL. After developing the masters for both devices, we used the masters to emboss layers of poly(dimethylsiloxane) (PDMS), punched holes for inlets and outlets, cleaned the surfaces with tape. If the device was attached to a glass coverslip it was treated with oxygen plasma and immediately sealed against a plasma-treated # 1.5 cover glass (24 x 50 mm Fisherbrand) to form a permanent seal.

**Measuring the bending rigidity of *P. mirabilis*, *V. paramaemolyticus*, and *E. coli* cells.** We used streak velocimetry to determine the profile of fluid flow rates in the central channel of the microfluidic device driven by gravity flow. We added fluorescently labeled 0.22 μm microspheres (Polysciences) diluted ~1:10000 in dd$H_2O$ containing 0.01% Brij-35 (Sigma) to the microfluidic channel and collected videos of the fluorescent beads moving through the channel at focal planes 2 μm apart. We analyzed the movies with custom-written code in Igor Pro 6.37 (WaveMetrics). Briefly, we applied a Gaussian blur and threshold to each frame and used the thresholded image to establish a region that was fit to a function based on a 2D Gaussian. We used the image exposure time and length of the streaks—taking into account the size of the microspheres—to calculate microsphere velocity. We mapped the velocity profile within the channel by analyzing several hundred microspheres. We binned the velocity data into a 3D matrix and fit it to a Poiseuille function, letting the velocity coefficient, height, and width float. The velocity coefficient was used as an input to the cell bending fitting function.

The system for gravity flow pumping (Fig. S14) consisted of two 6-mL syringes (Norm-Ject), one 60-mL syringe (BD), one 1-mL syringe (Norm-Ject), a ruler, and a VC-6 channel valve controller (Warner Instruments) connected to a VC-8 mini-valve system (Warner Instruments) that drives a three-way solenoid valve (The Lee Company). Syringe #1 (6-mL) was mounted to an immobile post, positioned 40 cm above the table

surface; this syringe was used to load cells. Syringe #2 (6-mL) was positioned 75-cm above the table surface, was connected to a stage that could be raised and lowered vertically, and was used to apply flow force in the device. Syringe #3 (60-mL) was mounted to an immobile post, positioned 75-cm above the surface of the table, and was used to apply an opposing flow force at the device outlet and to collect spent media/cells. We attached two-way valves, a blunt-end needle, and tubing to each syringe, including syringe #4 (1-mL). We joined the two 6-mL syringes using a Y-junction connector that led to the VC-8-mini-valve system inlet. The outlet of the valve system was connected to the microfluidic system. A ruler on an immobile post indicated the '0 position' (no pressure).

For cell bending experiments, we prepared filamentous vegetative cells and swarmer cells of *P. mirabilis* and *V. parahaemolyticus*; cells were normalized to an optical density (OD; $\lambda$=600 nm) of 1. Prior to starting a measurement, syringes 1 and 2 were flushed with dd$H_2O$ and fresh medium. Syringe 2 was filled with 4 mL of medium, syringe 3 was filled with 30 mL of dd$H_2O$, and syringe 4 was filled with 0.8 mL of dd$H_2O$. We added cells to syringe 1 and flowed them through the tubing until they reached the device outlet. To load the cells into the side channels of the device (from the central channel), we applied a suction force using the 1-mL syringe. After the side channels were loaded with cells, we adjusted the height of syringe 2 until no flow occurred in the device. Syringe 2 was then raised 7 cm from the no-flow position (a

288 height of 0 cm). We collected images of cells in the channel when syringe 2 was at
289 positions 0 cm and 7 cm using a Zeiss Axiovert 100 inverted microscope (Zeiss)
290 equipped with an iXon3 CCD (Andor), a 63X Plan-APOCHROMAT oil objective (Zeiss),
291 and Micro-Manager 1.4.16. After collecting cell-bending deflections for all loaded cells,
292 we expelled cells from the side channels, flowed liquid through the device for 15 s, and
293 reloaded the side channels with new cells.

294 We analyzed images to determine cell deflection under flow using custom
295 image-analysis software written in Igor Pro 6.37. The cell-bending model
296 (Supplementary Information) is a differential equation that lacks an analytical solution
297 and thus requires calculation of a numerical solution. To determine the bending rigidity
298 of cells, we wrote custom fitting code in Igor Pro 6.37 that uses a variety of input
299 parameters, including channel dimensions, fluid velocity, bending rigidity of the cell,
300 cell radius, and cell length. The function numerically calculates the maximum deflection
301 based on our model. This function is integrated into a fitting algorithm to find a least-
302 squares solution to a dataset of maximum deflections versus cell lengths with bending
303 rigidity as the fitting parameter.

304 Our model for bending a cell under flow is based on the mechanics model of a
305 suspended rod or cantilever bending under its own weight (see Section 4,
306 DERIVATIONS, below). Our experimental system was similar to that of Amir et al. (13).
307 Although laminar flow is perpendicular to the long axis of cells in this system, the

lateral deformations of cells that we measured were substantially larger (in our case, as large as 10 μm; compared to < 1 μm in Amir et al. (13). For this reason, many of the assumptions of the model presented by Amir et al. are not valid for our dataset. The model we developed to extract the bending rigidity of the bacterium takes into account the shape of the laminar flow profile, the angle of the cell against the flow profile, and the arc length of the cell (longer cells tend to fold over and do not penetrate as deeply into the flow profile). Our only major assumption is that the force of the bending moment at a particular point along a cell is not applied as an integration to the end of the cell, but is rather applied exactly one-half the distance (arc length) to the end of the cell. We found that models that take into account the full integration of the bending moment are computationally time-consuming and do not provide a substantial change in the calculated cell shape (data not shown).

## 2. FIGURES

**Figure S1. Reloadable microfluidic device design.** A cartoon depicting the entire microfluidic device including inlet, outlet, vacuum inlet, and the central bending chamber. Inset cartoon of the loading channels depicts the central bending chamber in which cells are loading into the 1st tier of channels using negative pressure. Inset cartoon of pillars (vacuum chamber): pillars are located in the vacuum chamber to ensure that the chamber does not collapse when the vacuum is applied. Green highlights the 1st layer of device (1-μm thick); black highlights the 2nd layer of device (25-μm thick).

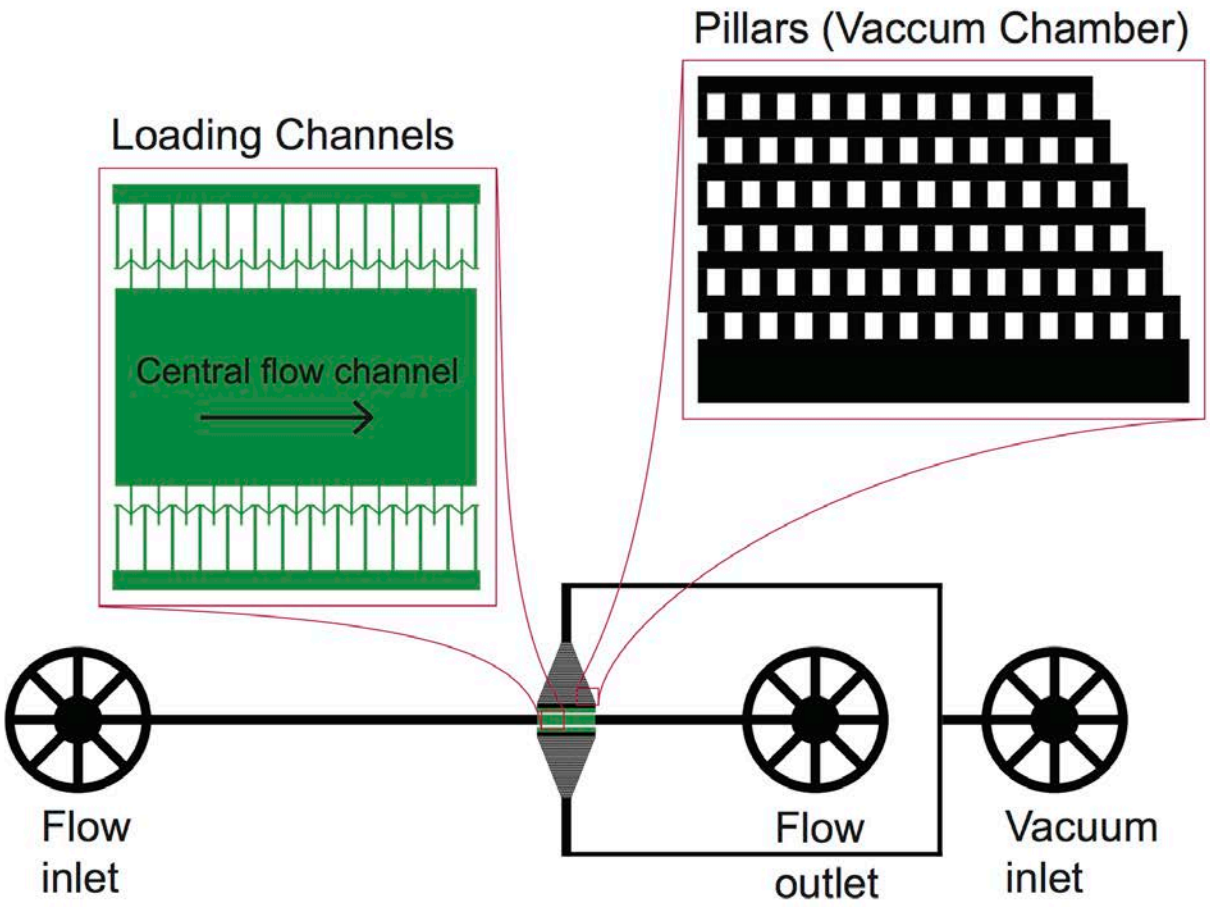


339

340 **Fig. S1**

341

**Figure S2. Deflection of vegetative filamented and swarmer cells immediately after flow-induced bending in microfluidic device.** Circles represent the deflection value of individual cells under fluid flow. Larger deflections (Figure S2C, E) indicate a decrease in cell stiffness. The black line represents a fit of our model (see SI methods, below) to the data to determine the flexural rigidity ($n > 200$ cells, from at least 2 independent experiments).

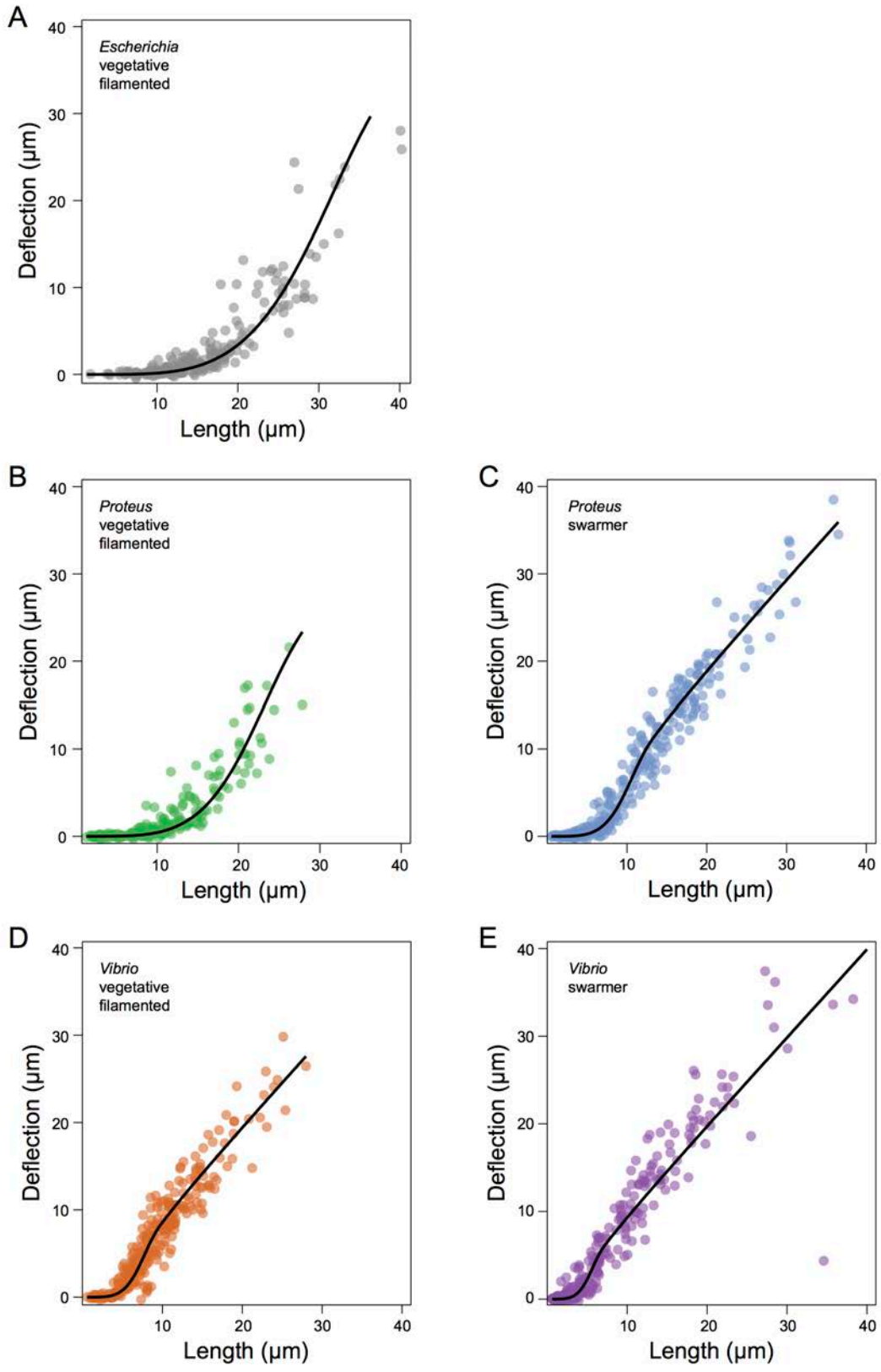


348

349 **Fig. S2**

**Figure S3. Division time for vegetative and swarmer cells grown at 30 °C.**

A) *V. parahaemolyticus* vegetative cells have a faster division time compared to *E. coli* and *P. mirabilis* cells. Data points indicated the division time of single vegetative cells ($n > 100$ cells from at least 3 independent experiments). Box plot is representative of the median, 1st and 3rd quartiles ("hinges"), and the 95% confidence interval of the median ("notches").

B) The onset of division in *P. mirabilis* swarmer cells is slower than *V. parahaemolyticus* cells but the time between division (division time interval) is reduced. Multiple division sites could be present on a single swarmer cell, and simultaneous division at 2 sites did occur. If simultaneous division occurred at two sites; one division time interval was designated as 0 min. The 2nd, 3rd, and 4th division time interval was calculated as (2nd division = 1st division time - 2nd division time). We analyzed $n > 100$ cells at the time of 1st division. Points represent the division time of single cells. Box plot depicts the median, 1st and 3rd quartiles ("hinges"), and the 95% confidence interval of the median ("notches").

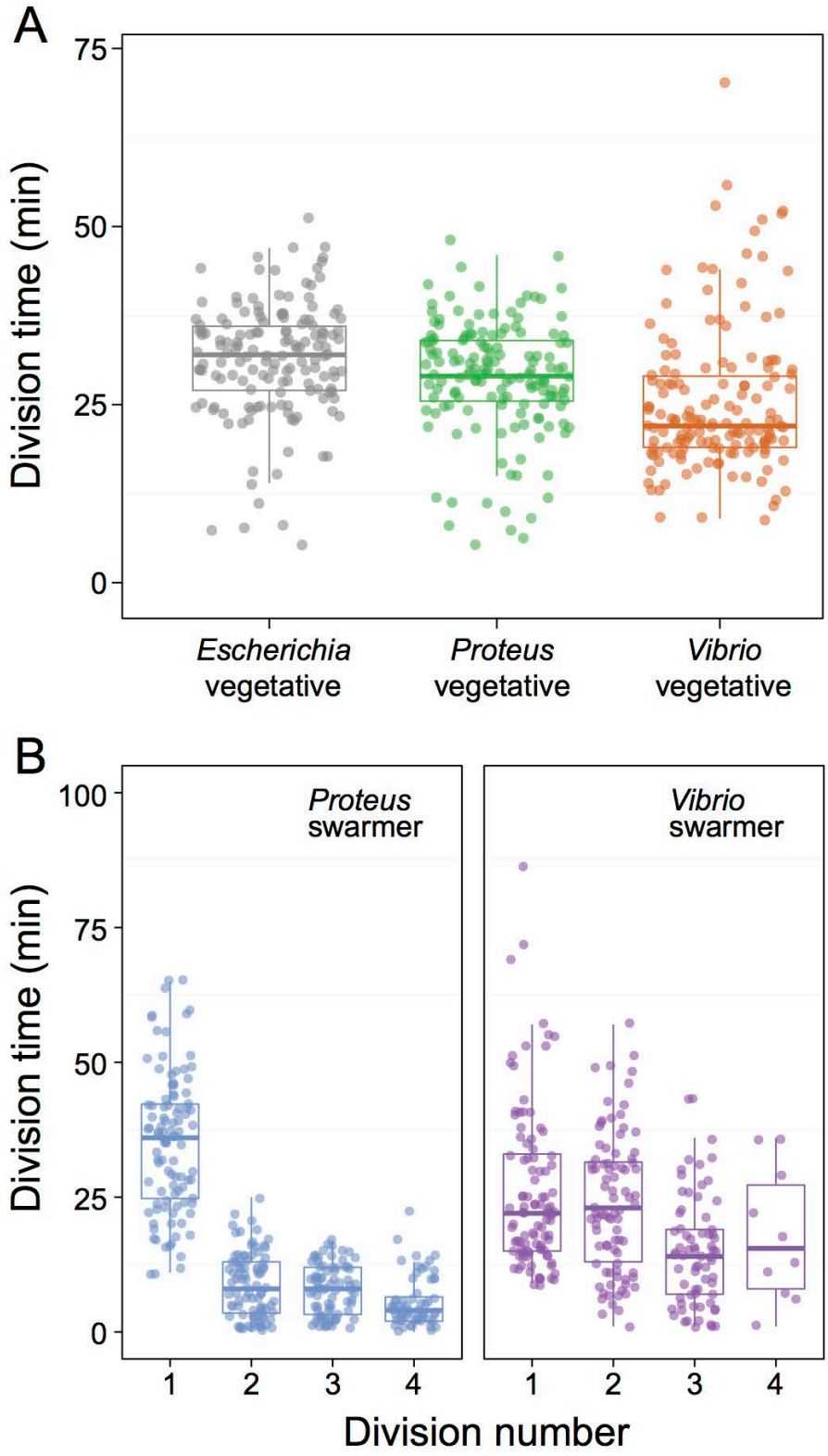


366

367 **Fig. S3**

**Figure S4. Flexural rigidity of *E. coli* is unaffected by treatment aztreonam or by an increase in flagella density.**

A) Bending rigidity is not affected by filamentation with aztreonam. Flexural rigidity of wild-type *E. coli* MG1655 cells filamented by expression of *SulA* (green) or treatment with aztreonam (gray). Flexural rigidity of cells was determined by fitting deflection data (Methods) from microfluidic-based bending assays. Error bars represent 95% confidence interval of fit to data ($n > 100$ cells, from at least 3 independent experiments).

B) Bending rigidity is not affected by an increase in number of flagella on the cell body. Data indicate the flexural rigidity of cells filamented with aztreonam: wild-type *E. coli* MG1655 (gray) and isolated *E.* coli MG1655 with an increased flagella density (red) (see Fig S4C). We determined the flexural rigidity of cells by fitting deflection data (Methods) from microfluidic-based bending assays. Error bars represent 95% confidence interval ($n > 100$ cells).

C) Immunofluorescence images of wild-type *E. coli* MG1655 (top panel) and *E. coli* MG1655 cells with increased flagella density (bottom panel) filamented with aztreonam. Flagella were labeled with anti-FliC primary antibody and an Alexa Fluor 488 conjugated secondary antibody. Scale bar = 10 μm.

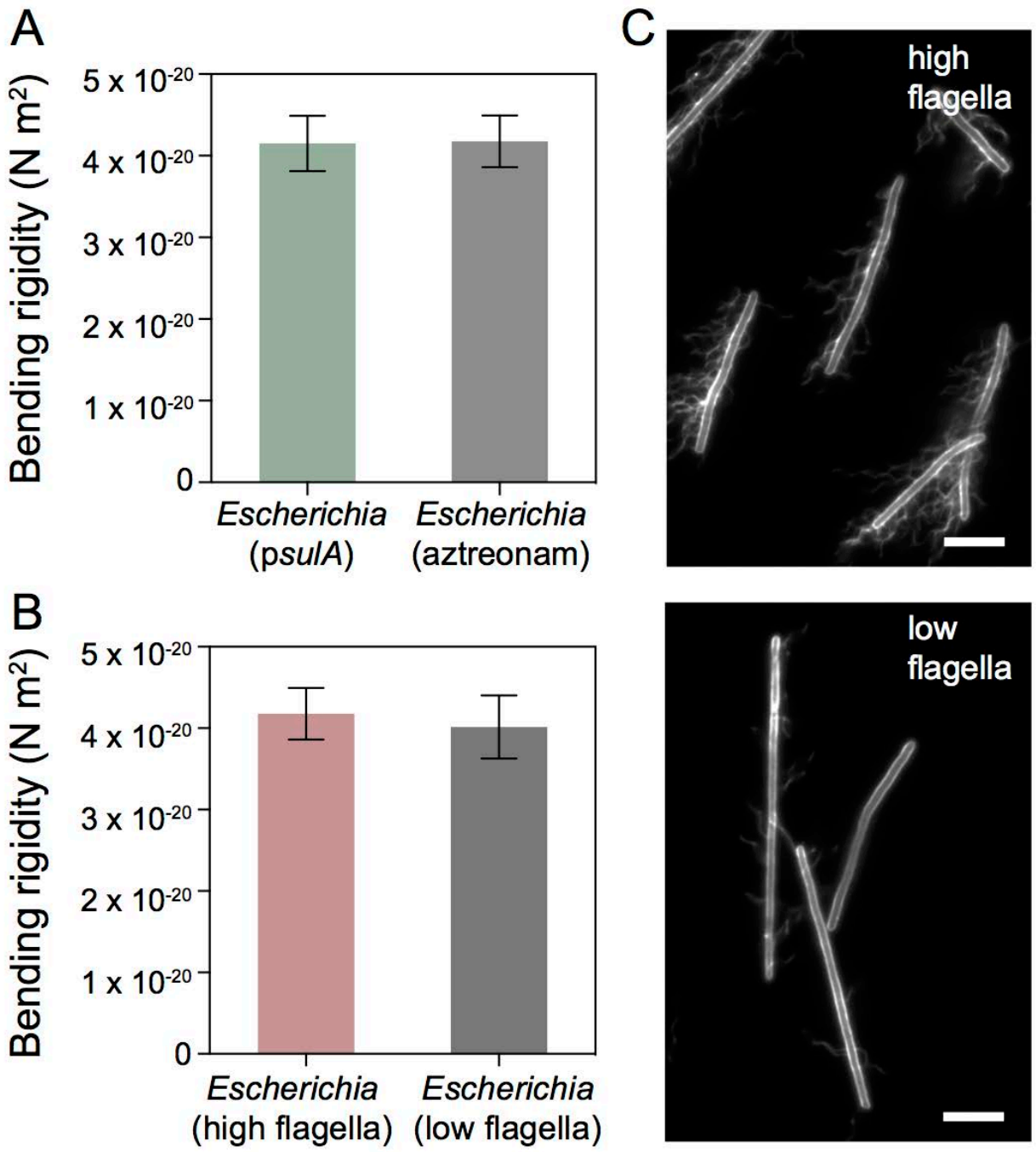


387

388 **Fig. S4**

389

390

**Figure S5. UPLC-MS data of muropeptides isolated from vegetative and swarmer cells.** Chromatograms of purified cell wall from *E. coli, P. mirabilis, V. parahaemolyticus* vegetative cells; and *P. mirabilis*, *V. parahaemolyticus* swarmer cells. We purified sacculi using the 24 h isolation method, digested them with mutanolysin, and analyzed them by UPLC-MS (10). Muropeptides were separated by UPLC using solvent A (water with 0.05% TFA) and solvent B [30% (v/v) methanol in water with 0.05% TFA]. Muropeptides were eluted from the column with a gradient of increasing solvent B at a flow rate of 0.2 mL/min; our gradient consisted of the following steps: hold 1 min at 1% B, ramp to 99% B over 60 min and hold at 99% B for 5 min; to prepare for the next sample we ramped back down to 1% B over 0.5 min and held at 1% B for 4.5 min. Table 1 lists the peaks that we identified and Figure 4 displays the quantification of peaks.

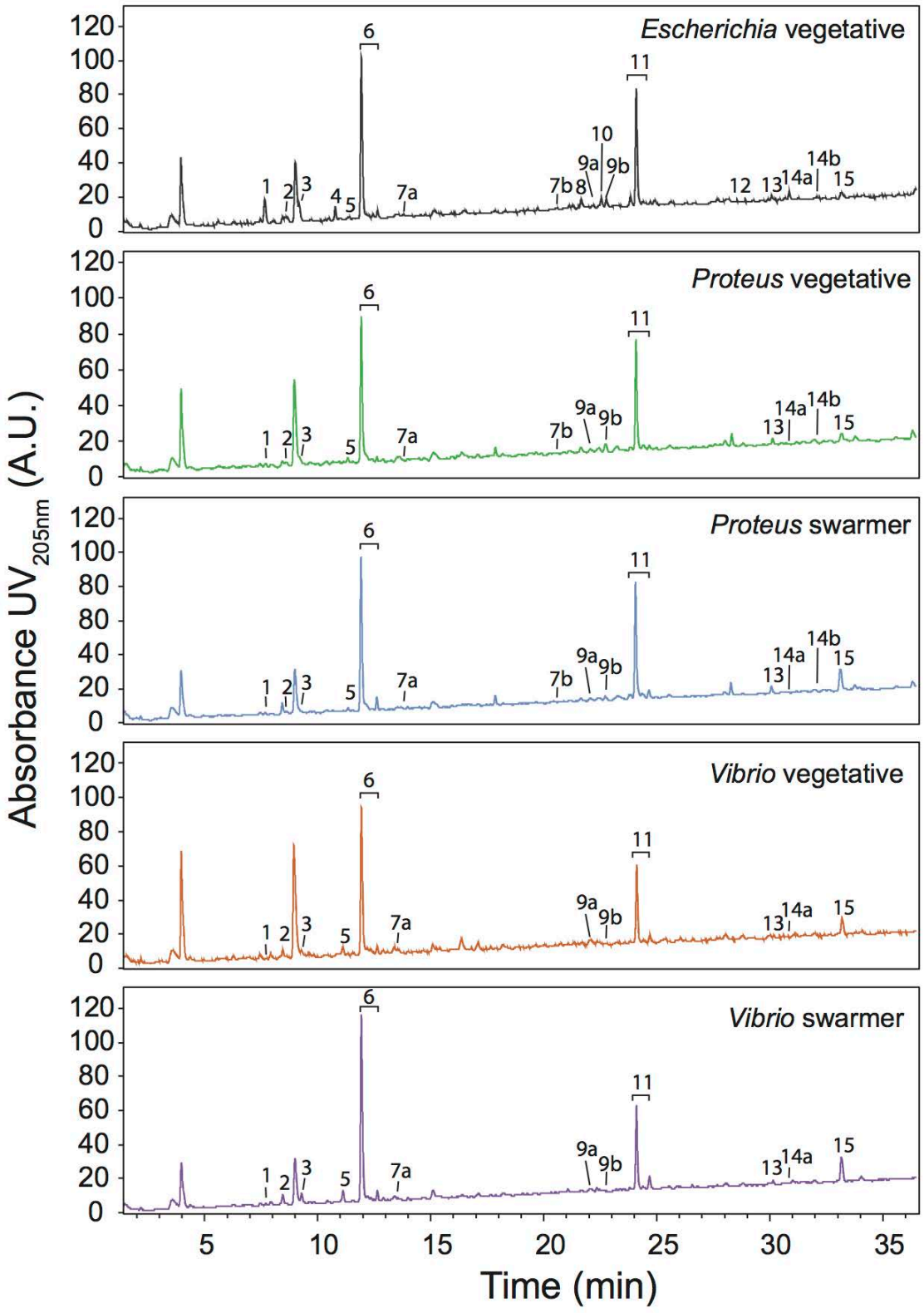


405

406 **Fig. S5**

**Figure S6. Determination of the muropeptide stem by MS/MS.** We analyzed the tetrapeptide peak (observed - 942.4036 m/z, calculated – 942.4155 m/z) by performing MS/MS on the parent ion to determine its amino acid composition. MS/MS confirmed that the *E. coli*, *P. mirabilis*, and *V. parahaemolyticus* muropeptide compositions are identical and consist of: L-Ala, D-Glu, meso-diaminopimelic acid, and D-Ala.

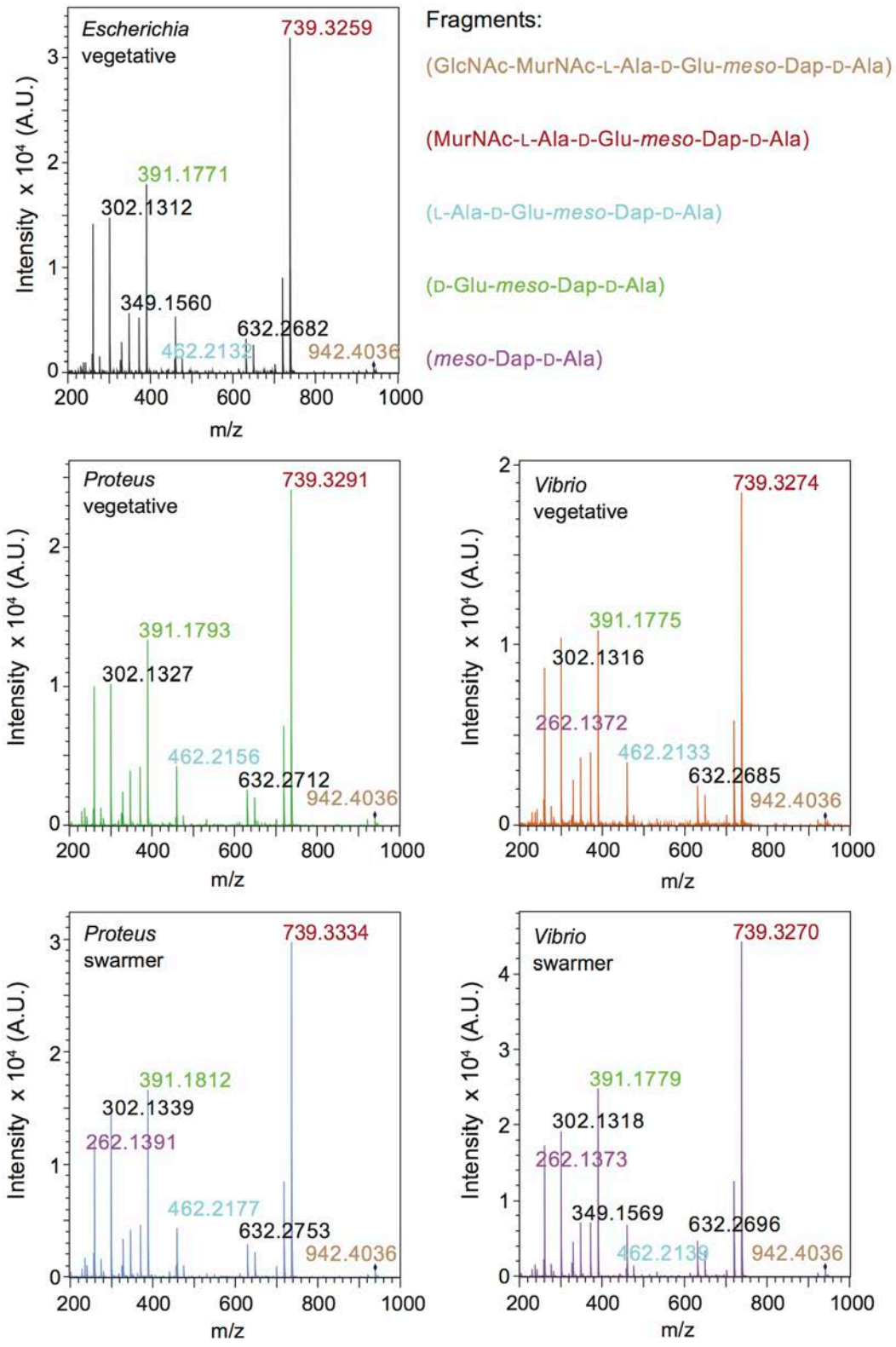
Escherichia
vegetative
739.3259
391.1771
302.1312
349.1560
632.2682
462.2139
942.4036
Fragments:
(GlcNAc-MurNAc-L-Ala-D-Glu-meso-Dap-D-Ala)
(MurNAc-L-Ala-D-Glu-meso-Dap-D-Ala)
(L-Ala-D-Glu-meso-Dap-D-Ala)
(D-Glu-meso-Dap-D-Ala)
(meso-Dap-D-Ala)
Proteus
vegetative
739.3291
391.1793
302.1327
462.2156
632.2712
942.4036
Vibrio
vegetative
739.3274
391.1775
302.1316
262.1372
462.2133
632.2685
942.4036
Proteus
swarmer
739.3334
391.1812
302.1339
262.1391
462.2177
632.2753
942.4036
Vibrio
swarmer
739.3270
391.1779
302.1318
262.1373
349.1569
632.2696
462.2139
942.4036
Intensity x 10⁴ (A.U.)
m/z

**Fig. S6**

**Figure S7. AFM images of isolated sacculi from *E. coli*, *P. mirabilis*, and *V. parahaemolyticus*.** A sample of dispersed sacculi was pipetted on freshly cleaved mica, dried under nitrogen gas, and imaged immediately. Imaging was performed using tapping mode AFM in ambient conditions (air). Images were collected at high resolution (512 x 512 pixels) with scan speed of 1 Hz. A) *E. coli* vegetative, B) *P. mirabilis* vegetative, C) *P. mirabilis* swarmer, D) *V. parahaemolyticus* vegetative, E) *V. parahaemolyticus* swarmer. Scale bar = 1 μm

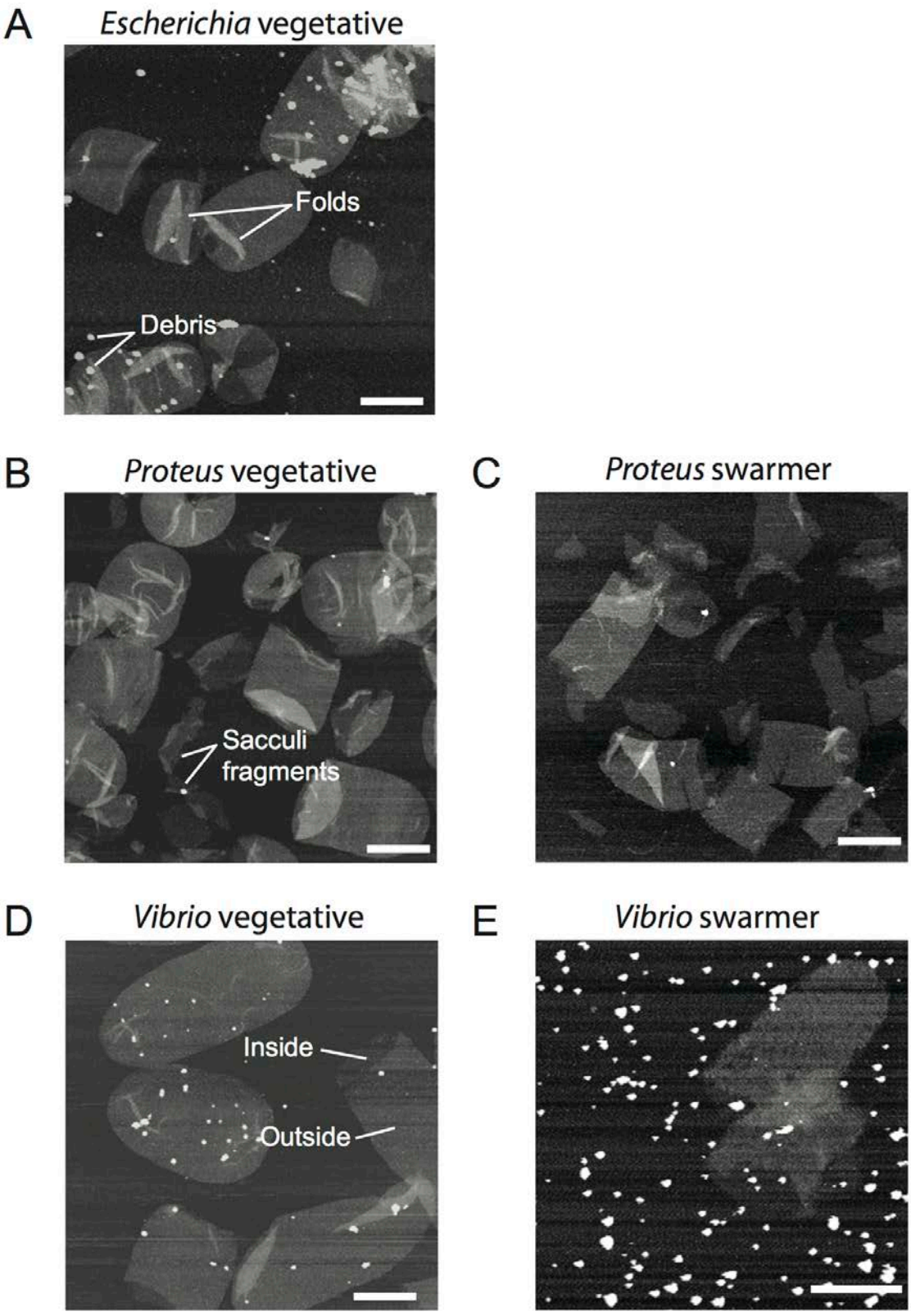


425

426 **Fig. S7**

**Figure S8. Electron cryotomography of *P. mirablis* vegetative and swarmer cells reveals decreased membrane stability.** *P. mirabilis* vegetative cells (A, B) have a smooth outer membrane and an increased distance between the inner and outer membrane (compared to swarmer cells). Swarmer cells (C-F) display a smooth lateral wall membrane (C, D) and a ruffled outer membrane near the pole (E, F) indicating a decrease in membrane stability. Representative features are labeled in figure panels A-F.

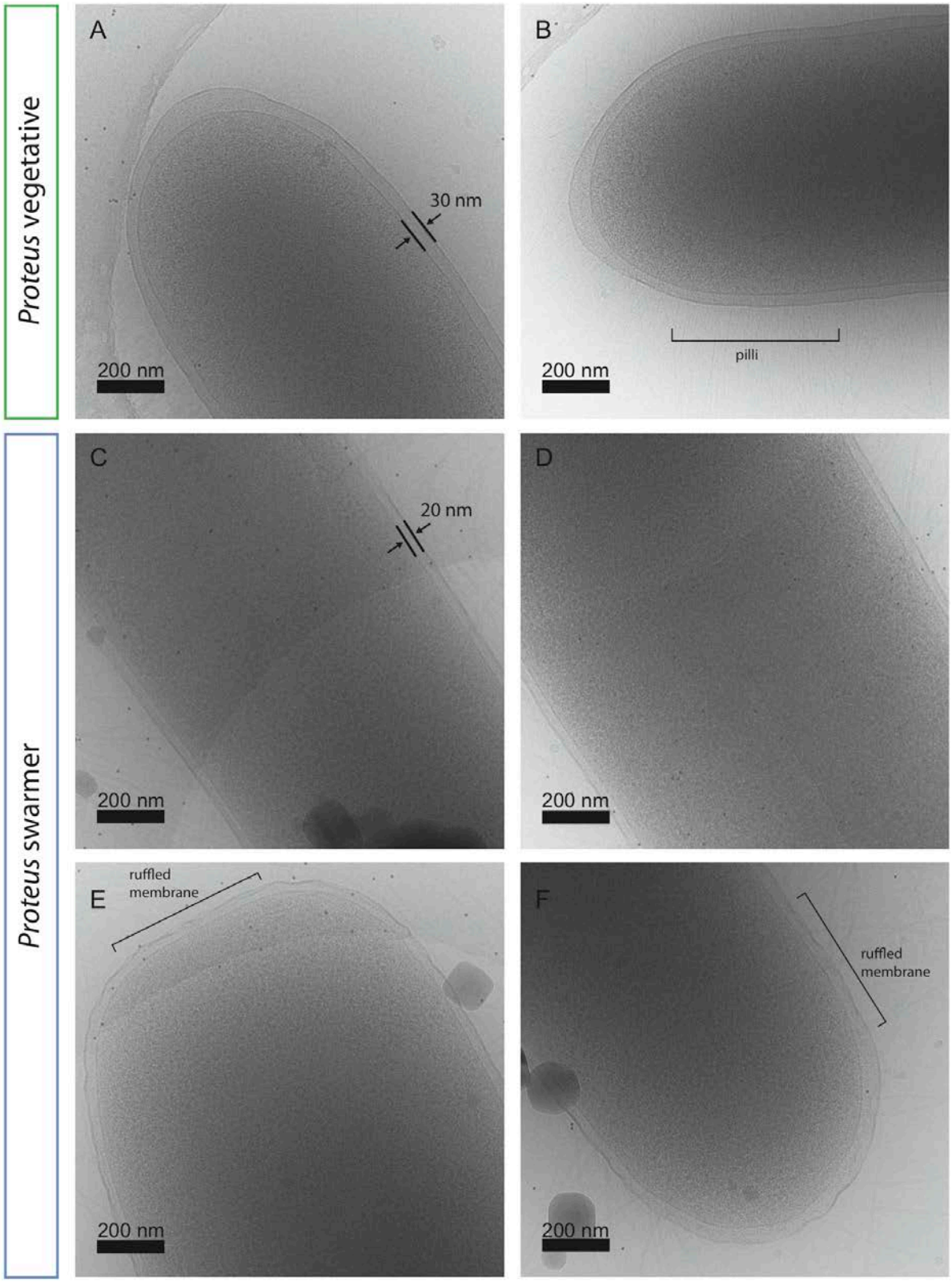


434

435 **Fig. S8**

**Figure S9. Electron cryotomography of *V. parahaemolyticus* vegetative and swarmer cells reveals cell membrane alterations and defects.** *V. parahaemolyticus* vegetative cells (A, B) have a smooth outer membrane that we also observed in *V. parahaemolyticus* swarmer cells (C); however some swarmer cells exhibited membrane blebs and vesicles (D-F). Ruptures in the cell wall (C) and variable cell diameter (E, F) were also observed. We were unable to determine if these features were the result of increased sensitivity to blotting pressures used when freezing the grids (D-F). Cells are suspended over a thiin carbon film containing circular holes that appear in some of the images (C, E, F).

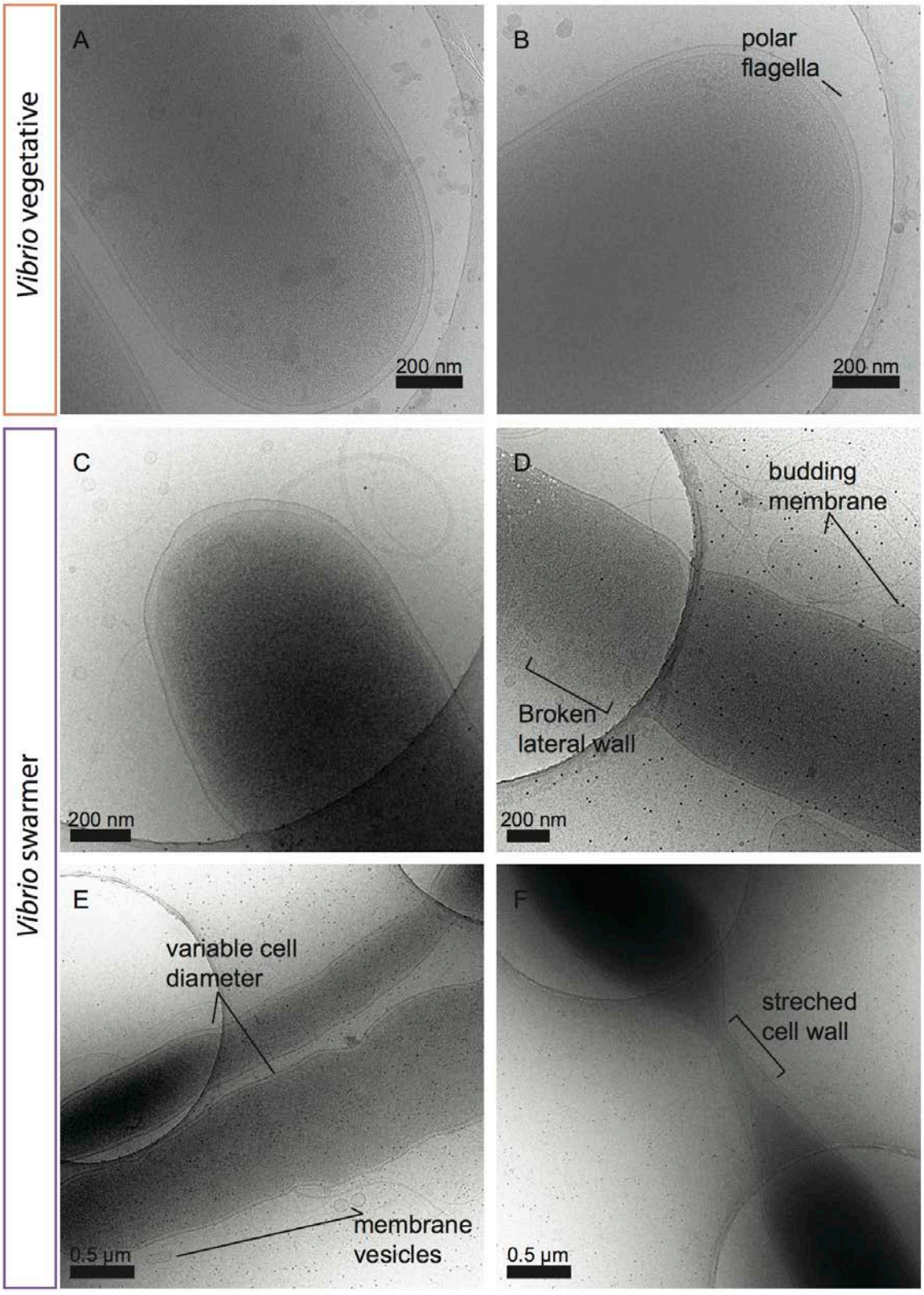
Vibrio vegetative
A
200 nm
B
polar
flagella
200 nm
Vibrio swarmer
C
200 nm
D
budding
membrane
Broken
lateral wall
200 nm
E
variable cell
diameter
membrane
vesicles
0.5 µm
F
streched
cell wall
0.5 µm

**Fig. S9**

**Figure S10. Elongation of vegetative filamented and swarmer cells during osmotic shock.** Cells were attached to the glass surface using Cell-Tak. Prior to performing osmotic experiments, we flowed fresh media through the device to remove any non-adhering cells from the surface. We flowed a hypertonic solution (1M NaCl) solution through the device until we saw visible cell plasmolysis. Immediately after, we flowed the hypotonic solution (dd$H_2O$) through the device until cells fully elongated. (A) Vegetative filamented cells and swarmer cells exposed to hypotonic (dd$H_2O$) and hypertonic (1M NaCl) conditions to alter cell length through increasing and decreasing turgor pressure, respectively. Scale bar = 10 μm. (B) A cartoon depicting the response of cell length during osmotic; arrows indicate the direction of turgor pressure in the cell.

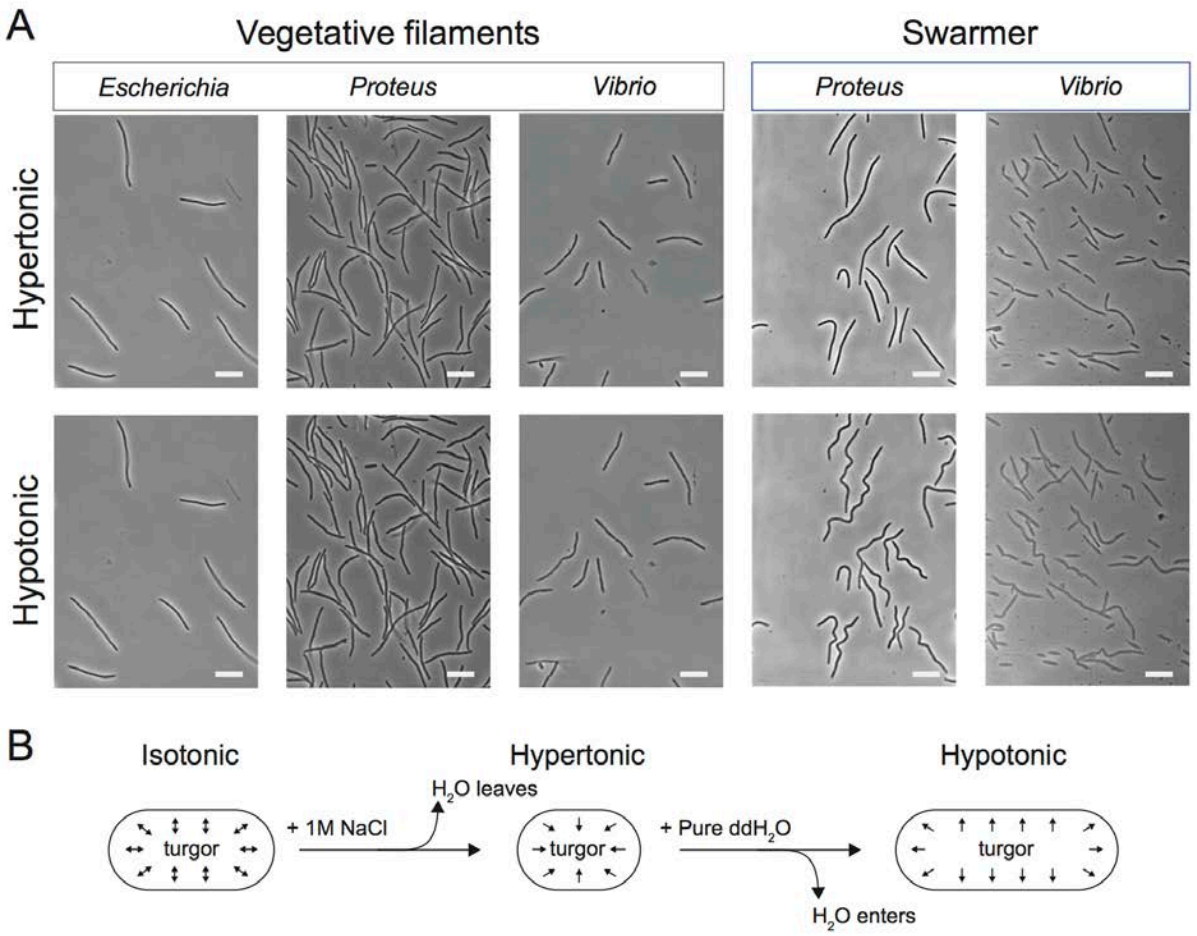
A
Vegetative filaments
Swarmer
Escherichia
Proteus
Vibrio
Proteus
Vibrio
Hypertonic
Hypotonic
B
Isotonic
Hypertonic
Hypotonic
turgor
+ 1M NaCl
H2O leaves
turgor
+ Pure ddH2O
H2O enters
turgor

**Fig. S10**

**Figure S11. A cartoon depicting the structure of the microfluidic flow device used in measurements of swarmer cells response to antibiotics.** A 250 μM thick layer of PDMS was applied to a cover glass. A 6 mm x 4 mm rectangular section of PDMS was removed using a scalpel and replaced with a nutrient media containing 2% (w/v) a warm solution of agarose. After the agarose had solidified and cooled, we pipetted 2 μL of a suspension of cells on the agarose surface, waited until the excess liquid was absorbed by the agarose, and inverted the agarose sandwiching the bacteria between the glass coverslip and agarose. The PDMS flow chamber was placed directly onto the PDMS coated coverglass ensuring the agarose pad was centered in the flow channel. A constant flow of nutrient media at 20 μL/min was supplied to the device using a syringe pump. Cell growth was monitored at 30 °C. Images were collected every 1 min for 3 h.

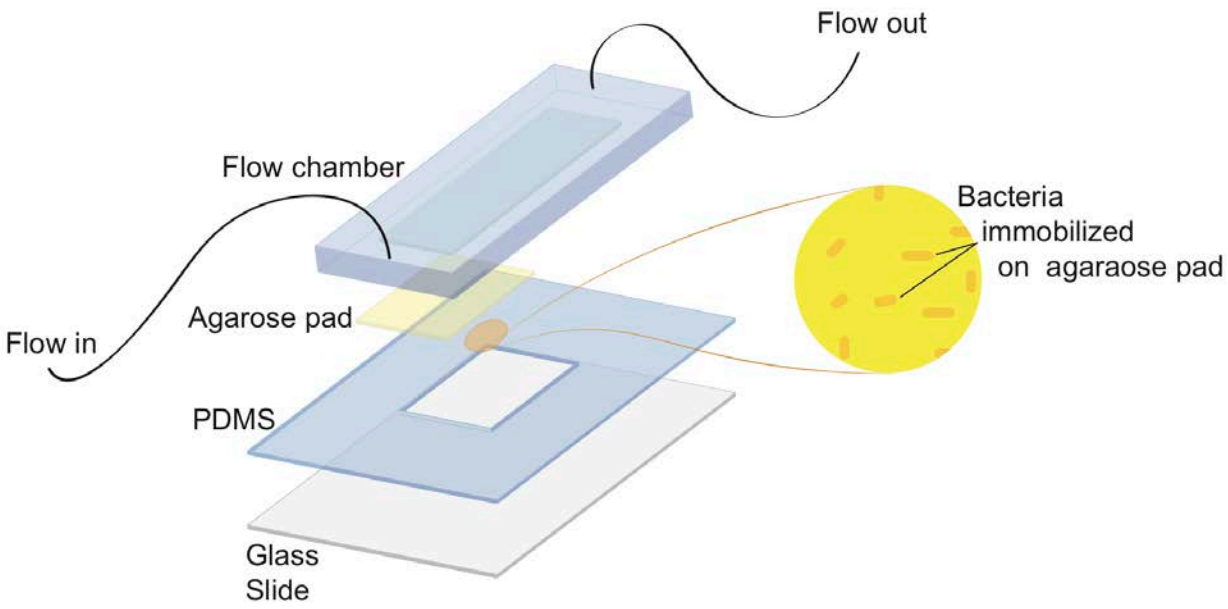
Flow out
Flow chamber
Bacteria
immobilized
on agaraose pad
Agarose pad
Flow in
PDMS
Glass
Slide

**Fig. S11**

**Figure S12. Sensitivity of cells to treatment with 1x MIC cephalexin.**

A) A phase contrast microscopy image showing *P. mirabilis* and *V. parahaemolyticus* cells treated with 1X MIC cephalexin in the microfluidic device shown in Fig S13. Time = 0 min depicts the time point cells immediately after the introducing cephalexin (1X MIC) to cells. At time = 180 min, we observed a higher frequency of swarmer cells compared to vegetative cells. Dead cells lose their phase contrast (they go from appearing dark to light/transparent). Membrane blebbing and filamentation are a direct result of cephalexin treatment. Scale bar = 10 μm.

B) A cartoon depicting the time course of cells treated with cephalexin. Time progresses from left to right. The ring structure represents the division protein FtsZ.

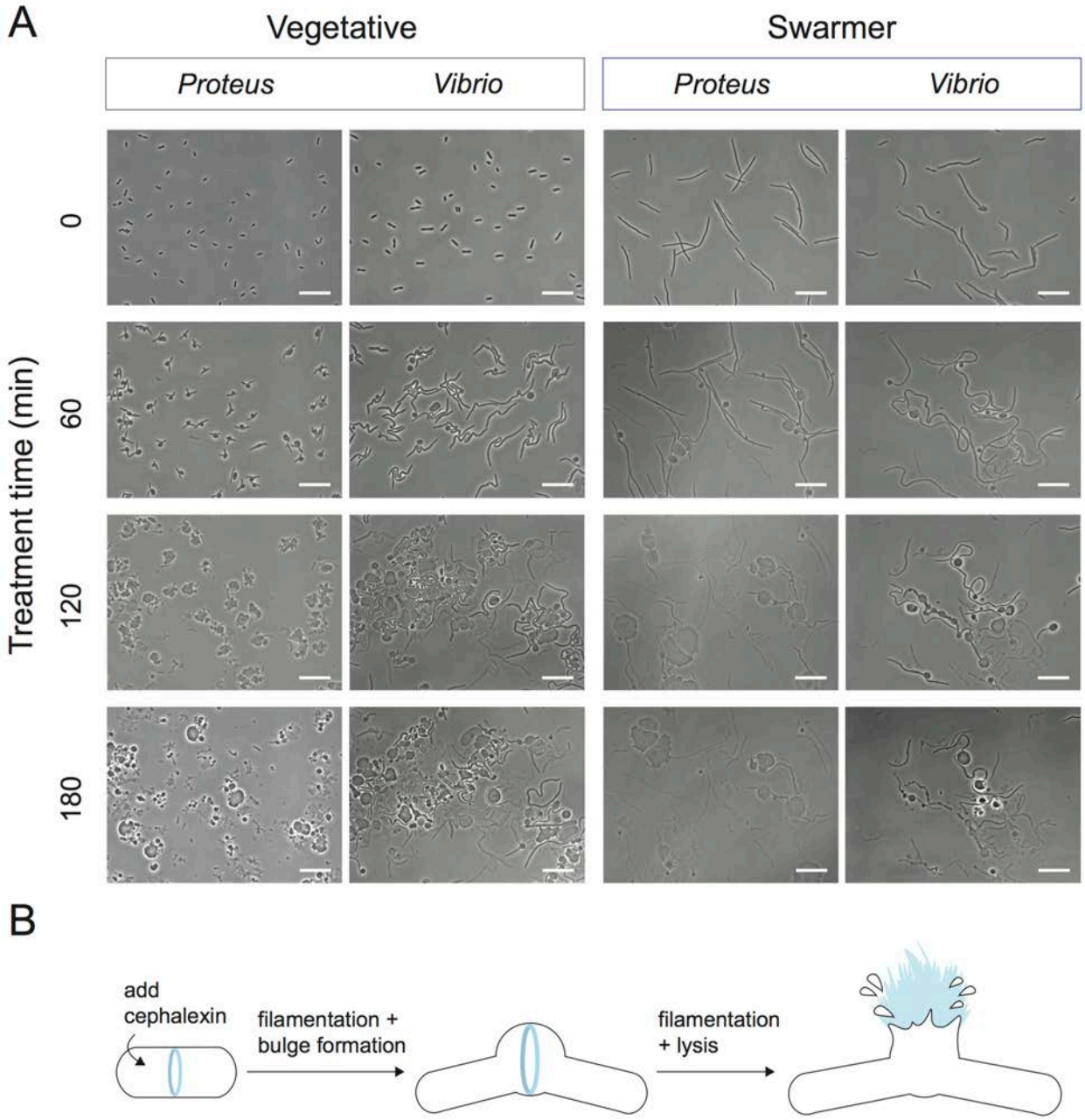


504

505 **Fig. S12**

**Figure S13. No significant change in the growth rate of cells treated with β-lactams.** Vegetative and swarmer cells do not show a significant change in growth rate when treated with β-lactam antibiotics. We monitored the growth rate of vegetative exponential phase cells and swarmer cells for 15 min in the microfluidic growth device described in Figure S11. A) A plot of cell growth in the presence of cephalexin (1X MIC); and B) a plot of cell growth in the presence of penicillin G (1X MIC) [$n > 40$ cells, from at least 2 independent experiments]. The box plot depicts the median, 1st and 3rd quartiles ("hinges"), and the 95% confidence interval of the median ("notches"). Black dots represent outliers in data.

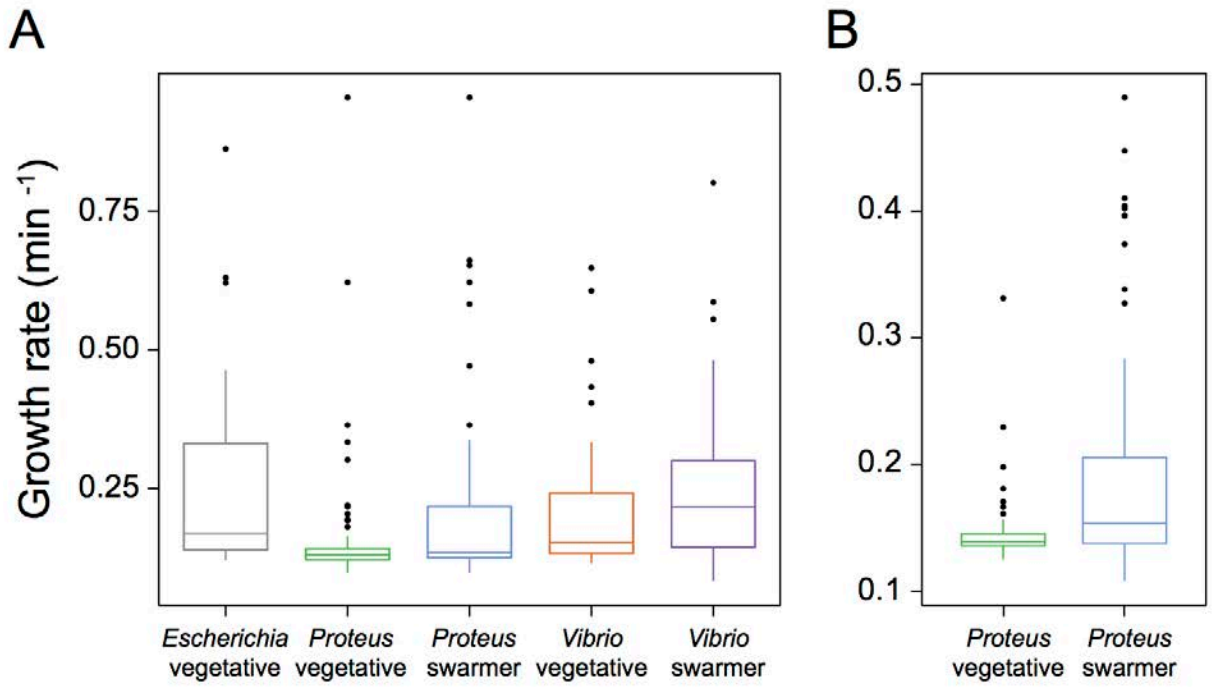
A
B
Growth rate (min -1)
0.75
0.50
0.25
0.5
0.4
0.3
0.2
0.1
Escherichia vegetative
Proteus vegetative
Proteus swarmer
Vibrio vegetative
Vibrio swarmer
Proteus vegetative
Proteus swarmer

**Fig. S13**

**Figure S14. Gravity flow setup used with the reloadable cell bending microfluidic device.** An image of the gravity flow system we used for precisely delivering fluids at user-defined flow rates for bending measurements. We assembled the flow system next to an inverted microscope; a VC-6 channel valve controller is located outside of image. See methods for operation of the system.

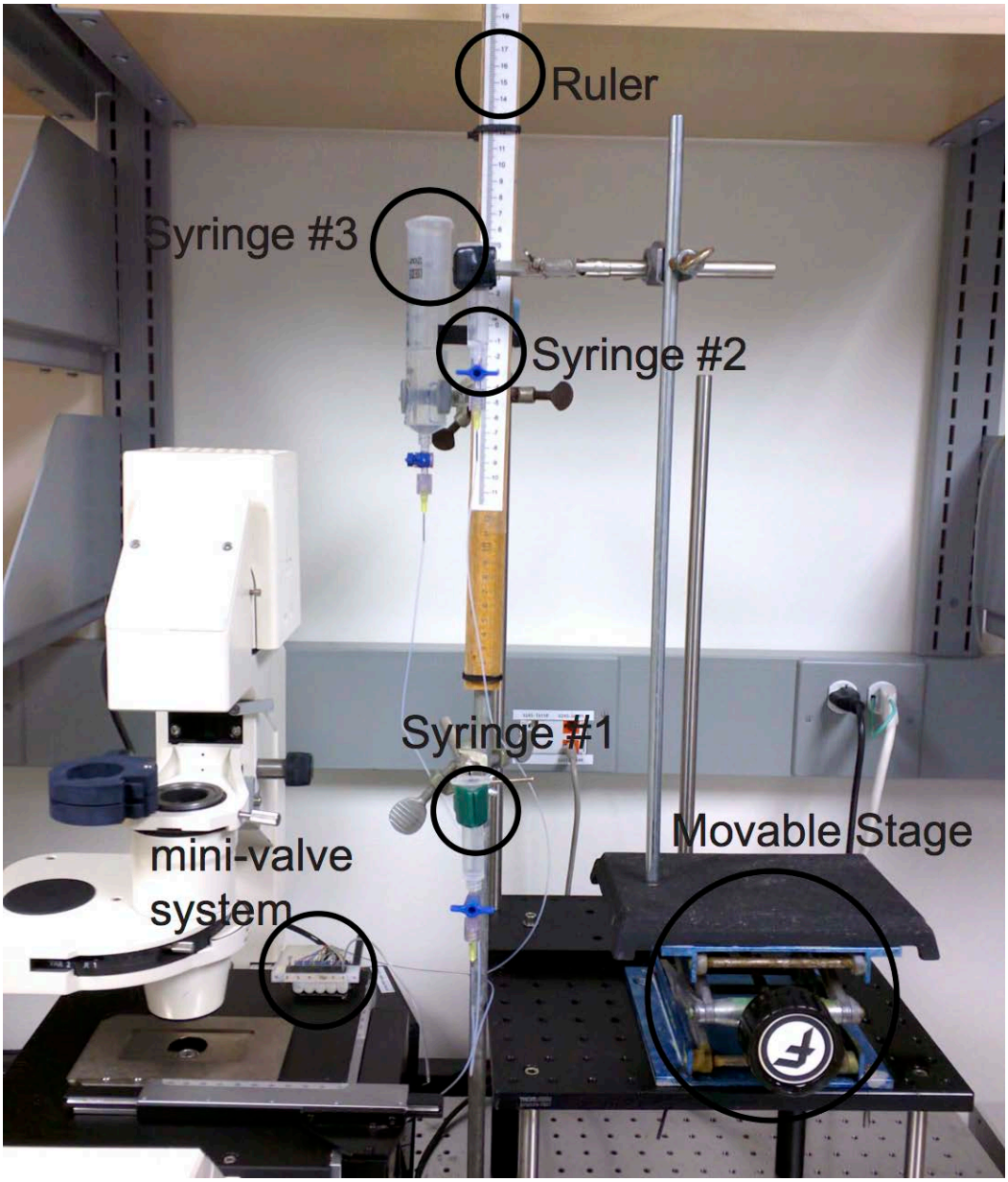
Ruler
Syringe #3
Syringe #2
Syringe #1
Movable Stage
mini-valve
system

**Fig. S14**

## 3. TABLES

**Table S1. Muropeptides analyzed by UPLC-MS in positive ion mode.** Identification of muropeptides by MS. We identified muropeptides within (± 0.01 m/z) of the calculated muropeptide mass values. Identified peaks corresponded to mass values with following adducts ($1H^+$, $2H^+$, and $3H^+$). MS peaks were used to identify and quantify area under curve of UPLC $UV_{205nm}$ peaks (Figure S8).

| Peak | Retention time (min) | Calculated mass | | | Length of stem peptides |
|---|---|---|---|---|---|
| | | H+ | 2+ | 3+ | |
| 1 | 7.7 | 871.3784 | 436.1892 | 291.1261 | Tri |
| 2 | 8.6 | 928.3999 | 464.6999 | 310.1333 | Tetra-Gly(4) |
| 3 | 9.2 | 699.2936 | 350.1468 | 233.7645 | Di |
| 4 | 10.8 | 999.4370 | 500.2185 | 333.8123 | Penta-Gly (4) |
| 5 | 11.6 | 1243.5202 | 622.2601 | 415.5067 | Tri-Tri (-DS) |
| 6 | 12 | 942.4155 | 471.7078 | 314.8052 | Tetra |
| 7a | 13.6 | 1723.7102 | 862.3551 | 575.2367 | Tri-Tri |
| 7b | 20.6 | 1723.7102 | 862.3551 | 575.2367 | Tri-Tri |
| 8 | 21.3 | 1851.7970 | 926.3985 | 617.9323 | Tetra-Tetra-Gly(4) |
| 9a | 21.7 | 1794.7756 | 897.8878 | 598.9252 | Tetra-Tri |
| 10 | 22.6 | 1922.8341 | 961.9171 | 641.6114 | Tetra-Tetra-Gly (5) |
| 9b | 22.8 | 1794.7756 | 897.8878 | 598.9252 | Tetra-Tri |
| 11 | 24.1 | 1865.8127 | 933.4063 | 622.6042 | Tetra-Tetra |
| 12 | 28.6 | 2846.2313 | 1423.6156 | 949.4104 | Penta-Gly(5)-Tetra-Tetra |
| 13 | 30.1 | 2789.2098 | 1395.1049 | 930.4033 | Tetra-Tetra-Tetra |
| 14a | 30.7 | 1774.7402 | 887.8701 | 592.2467 | anhydro Tetra-Tri |
| 14b | 32.1 | 1774.7402 | 887.8701 | 592.2467 | anhydro Tetra-Tri |
| 15 | 33.2 | 1845.7865 | 923.3932 | 615.9288 | anhydro Tetra-Tetra |

## 4. DERIVATIONS

### Derivation of the equation(s) describing the behavior of a rod-shaped bacterium bending under laminar fluid flow

The model for bending a cell is based on the mechanics model of a suspended rod (cantilever) bending under its own weight (Fig. S15). Analytical solutions have been developed for this model, but are not adequate to describe the large deformations measured in our setup.

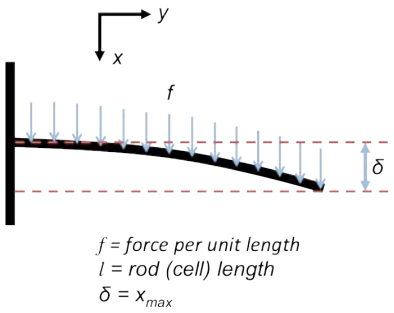


**Figure S15.** Schematic model of a cantilever or cell bending under its own weight.

### General bending of cantilevered rod equation

At each point along the cantilevered rod or cell, there is an external stress and an internal stress. The external stress is the application of force due to gravity or forces from the fluid. The internal stress, or response, comes from the mechanical properties of the rod, which is what we are interested in probing. By setting these two stresses equal to each other, we can relate the two and extract meaningful information about the material properties of the rod. First we will consider how the internal stress is calculated.

*Internal Stress*:
It is helpful to consider that along every point of the rod there is an associated curvature, $\kappa$, defined as the inverse of the radius, $R$, formed by a circle at that point. The curvature is related to the infinitesimal angle, $\Delta\theta$, and infinitesimal arc length, $\Delta y$, at the point of interest (see Fig. S16).

$$\kappa = \frac{1}{R} = \frac{\Delta\theta}{\Delta y} \tag{1}$$

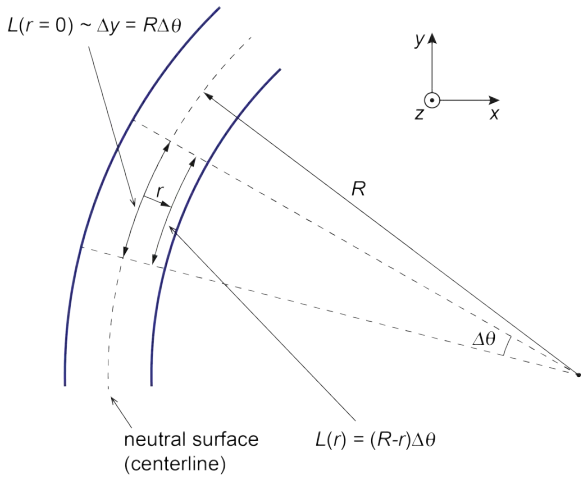


**Figure S16.** Schematic of a curved geometry at each point along the rod (cell). Note that moving away from the centerline by a distance, $r$, shortens the arc length made by $\Delta\theta$. The image is rotated with respect to Figure S15 in order to reflect the final geometry we are interested in but the coordinate system is the same.

The extensional strain, $\varepsilon$, is the ratio of extension and length and is defined as follows at each point within the cross-section:

$$\varepsilon = \frac{L(r) - L(0)}{L(0)} \tag{2}$$

We can substitute the information from Figure S16 into Equation 2:

$$\varepsilon = \frac{(R - r)\Delta\theta - R\Delta\theta}{R\Delta\theta} = -\frac{r}{R} \tag{3}$$

Equation 3 relates extensional strain to the local radius of curvature, $R$, and the position within the rod (cell) cross-section, $r$. Tensile strain, $\sigma$, is the force per unit area and is related to extensional strain by the Young's Modulus, $Y$:

$$Y = \frac{\sigma}{\varepsilon} \tag{4}$$

which traditionally has units of Pascals (Pa), or N $m^{-2}$. Substituting Equation 3 into 4:

$$\sigma = -\frac{Yr}{R} \tag{5}$$

Equation 5 relates the tensile strain to Young's Modulus, position in the cross-section, $r$, and local radius of curvature, $R$. Assuming a linearly elastic material, the total internal

force in a particular cross section must be equal to zero and is, therefore, the summation of all tensile strains multiplied by the total area:

$$F_{tot,\text{int}} = \sum_i F_i = \sum_i \sigma_i A_i \approx \int \sigma \, dA = 0 \tag{6}$$

The total internal bending moment, *M*, however, is not zero. This is because the directional aspect of the bending moment, *r*, counteracts the negative sign of the tensile strain when moving from compression to extension (i.e. in Figure S16 moving from the right part of the rod to the left). The *total* internal bending moment for a cross-section is defined as:

$$M_{tot,\text{int}} = -\sum_i F_i r_i = -\sum_i \sigma_i A_i r_i = -\int \sigma r \, dA \tag{7}$$

Substituting in equation 5:

$$M_{tot,\text{int}} = \frac{Y}{R} \int r^2 \, dA \tag{8}$$

The area moment of inertia (second moment of inertia), *I*, is defined as:

$$I = \int r^2 \, dA \tag{9}$$

Substituting Equation 9 into Equation 8 gives us:

$$M_{\text{int}} = \frac{YI}{R} \tag{10}$$

Equation 10 describes the moment of inertia of a cross-section of the cell. For clarity, we rewrite it as a function of position in the *y*-direction (see Figs. S15 & S16 for coordinate system).

$$M_{\text{int}}(y) = \frac{YI}{R(y)} \tag{11}$$

The area moment of inertia for a hollow disc cross-section can be derived to:

$$I = \pi r_{cell}^3 h \tag{12}$$

where $h$ is the thickness of the disc (cell wall thickness) and $r_{cell}$ is the radius of the rod (cell). This quantity, $I$, will be useful later when calculating the Young's Modulus of the cell wall from the flexural rigidity ($YI$).

*External Stress*:

Equation 11 provides a relationship between the local internal bending moment, the flexural rigidity, and the radius of curvature within the rod (cell) for a given cross-section. However, these are internal stresses. The external stresses have to be balanced, meaning we have to write the bending moment for the external force on the rod (cell) at each point. For now, we will assume that force is evenly distributed along the rod (cell).

At any point along the cell, $y$, the external bending moment, $M_{ext}$, (Equation 15) is the total load of the force along the remainder of the cell (Equation 13) times the location of the centroid of that force, $\bar{y}$, (Equation 14):

$$F_{y \text{ to } l} = f(l - y) \tag{13}$$

$$\bar{y} = \tfrac{1}{2}(l - y) \tag{14}$$

$$M_{\text{ext}}(y) = F_{y \text{ to } l}\,\bar{y} = \tfrac{1}{2} f(l - y)^2 \tag{15}$$

where $f$ is the force per unit length and $l$ is the length of the rod (Figure S17). Note that the bending moment is really a torque at that particular point along the rod.

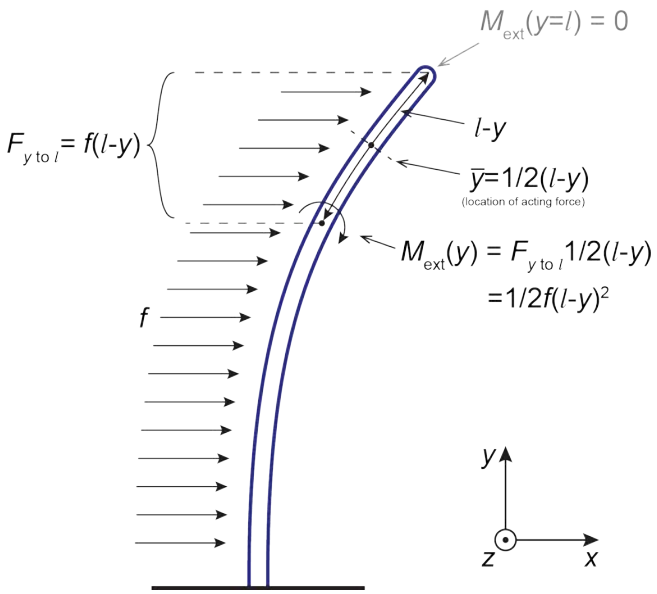


**Figure S17.** Schematic showing the derivation of the external bending moment for a cantilevered rod (cell) with a constant force, $f$, along the rod. The bending moment shown, $M(y)$, is for any arbitrary point along the cell and goes to zero at the tip (when $y = l$).

Now we balance the internal and external bending moments at each point along the rod ($M_{int}(y) = M_{ext}(y)$) and solve for the curvature, yielding the equation:

$$\frac{1}{R(y)} = \frac{\frac{1}{2}f(l-y)^2}{YI} \tag{16}$$

We are interested in the $x$-position (deflection) of the rod at each point along $y$. This can be accomplished by realizing $1/R(y)$ is the local curvature and the curvature of any function is defined as:

$$\frac{1}{R(y)} = \frac{\frac{d^2x}{dy^2}}{\left(1+\left(\frac{dx}{dy}\right)^2\right)^{\frac{3}{2}}} \tag{17}$$

where here we implement the derivative with respect to $x$ ($1/R(y)$ and $1/R(x)$ are equivalent) in order to get a final function with respect to $x$. Setting equation 16 and 17 equal to each other yields the general differential equation:

$$\frac{d^2y}{dx^2} = \frac{M_{\text{ext}}}{YI}\left(1 + \left(\frac{dy}{dx}\right)^2\right)^{3/2} \quad (18)$$

where:

$$M_{\text{ext}} = \tfrac{1}{2}f(l-y)^2 \quad (19)$$

Assuming the first derivative is zero (appropriate *only* for small deflections), yields the following function of $y$.

$$x(y) = \frac{fy^2(y^2 - 4ly + 6l^2)}{24YI} \quad (20)$$

The maximal deflection, $x_{\max}$, is at the tip, where $y = l$, yielding the equation:

$$x_{\max} = \frac{fl^4}{8YI} \quad (21)$$

Equation 21 describes the maximal tip deflection in a rod (cell) with very small deformations and a constant force along the cell. This equation was derived in the supplementary material from Amir et al. (13).

**Derivation of models with fewer assumptions:**

The geometry of our system (Fig. S16) is quite similar to what is shown in Fig. S15, but there are three main factors that must be taken into account when modeling at large deformations:

(1) The solution up to this point (Equations 19, 20, & 21) does not take into account the arc length of the cell as it bends. In other words, the analytical solution makes it seem that when the cell bends significantly, the length of the cell actually gets longer.
(2) In a laminar flow system, the force ($f$) along the cell is not uniform; it changes based on the laminar flow profile.
(3) There must be some sort of attenuation of the force on the cell as it bends substantially and its orientation with respect to the flow becomes non-perpendicular. *This effect is not taken into account with the model presented here since it is too computationally intensive.*

(1) *Addressing the arc length:*

We need a model that takes into account the fact that the tip of the cell moves downward (-*y* direction) as the cell is bent substantially. What is needed is a term that takes into account the arc length of the cell, *s*, which, for any differentiable function starting from $y = 0$ is:

$$s(y) = \int_0^y \sqrt{1 + \frac{dx}{dy}}\, dy \tag{22}$$

Replacing *s* with *y* in the bending moment in Equation 19 gets us:

$$M_{\text{ext}}(y) = \tfrac{1}{2} f\big(l - s(y)\big)^2 \tag{23}$$

Addition of the arc length into the bending moment means the differential equation (Equation 18) is no longer amenable to an analytical solution. It will need to be solved numerically. Equations 18 & 23 are the basis for the model (B) used to calculate maximum deflections of cells in the microfluidic device. The numerical solution is discussed later in this document.

(2) *Addressing the non-uniform laminar flow profile:*

The laminar flow profile (described by the Poiseuille flow equation) provides the velocity vector along the geometry of the device. Hence, *f* is actually a function of a number of parameters including the characteristic flow velocity, $v^*$, chamber width, *w*, chamber height, *h*, as well as cross-sectional area of the cell$\pi$.

$$v = v^* \left[ \frac{z}{2h}\left(1 - \frac{z}{h}\right) - 4 \sum_{n=0}^{\infty} \frac{\sin\left[(2n+1)\frac{\pi z}{h}\right]}{(2n+1)^3 \pi^3} \left( \frac{\cosh\left[(2n+1)\pi\left(\frac{y}{h} - \frac{w}{2h}\right)\right]}{\cosh\left[(2n+1)\frac{\pi w}{2h}\right]} \right) \right] \tag{24}$$

$$f(y) = 4\pi\eta r \left.\frac{\partial v}{\partial z}\right|_{y,\ z=r} \tag{25}$$

where $\eta$ is the viscosity and *r* is the radius of the cell. The partial derivative of velocity with respect to *z* in Equation 25 is calculated at a given *y*-position and at a *z*-position close to the surface (e.g. where *z* equals the radius of the cell) (14). We use a *z*-position of 0.5 μm in all of our calculations. Note that a practical value of *n* for the summation in Equation 24 is approximately 10, which is the default value in our calculations.

This complicated flow function makes the model for cell-bending untenable to an analytical solution—although Amir, et al. did use an approximate constant force for their calculations to obtain a reasonable result.

It is important to note that the relationships shown in Figure S17 are true only when there are small deformations and the force along the rod is uniform. In order to take into account a non-uniform force, we must calculate the bending moment along the cell at each point. Ignoring, for now, the arc length, the general definition of the bending moment is:

$$M_{\text{ext}}(y') = F_{y'\text{to }l}\, y_c(y') = \int_{y'}^{l} f(y)dy \frac{\int_{y'}^{l} f(y)(y-y')dy}{\int_{y'}^{l} f(y)dy} = \int_{y'}^{l} f(y)(y-y')dy \quad (25)$$

where $y'$ is referring to the point at which the bending moment is being calculated and $y_c$ is the centroid force coordinate (effective position of the applied force).

If $f(y)$ is assumed to be constant, as in Figure S3, then Equation 25 simplifies to:

$$M_{\text{ext}}(y') = f\int_{y'}^{l}(y-y')dy = \tfrac{1}{2}f(l-y')^2, \quad (26)$$

and is the same result as in Equation 15 (model **A1**), which we got by inspection. In our system, however, the force is not constant along the length of the cell and the force must remain a function of $y$, as in Equation 25. The addition of an arc length further complicates the equation:

$$M_{\text{ext}}(y') = \int_{s'}^{l} f(y)(s-s')ds \quad (27)$$

where $s'$ is the arc length at $y'$. Although it is possible to construct a solution using Equation 27, we assume that the force for a given bending moment is calculated and applied at one half the arc distance to the end of the cell.

For the 'B' model, the bending moment is:

$$M_{\text{ext}}(y) = \tfrac{1}{2}f(y_{\text{c}})(l-s(y))^2, \quad (28)$$

where

$$y_{\text{c}} = y \,@\, \tfrac{1}{2}\big(l-s(y)\big) + s(y). \quad (29)$$

The value $y_c$ is calculated numerically.

**Models and Numerical solution methods:**

The various models and governing equations are presented schematically in Figure S18. They are solved using a procedure file written for Igor Pro 6.37 (Wavemetrics, Inc.).

A-models (not used in manuscript):

The 'A' models are governed by Equations 20 and 21 and are not full solutions to the differential equation (Equation 18) because the solutions disregard the first derivative and simplify the bending moment. Furthermore, the forces applied are approximate.

*Model A1:* A1 is governed by Equation 21 and follows a simple fourth-order exponential.

*Model A2:* A2 is governed by Equation 20, but the arc length is numerically calculated using Equation 22. The $x_{max}$ value is found where the cell length, $l$, equals the arc length.

B-model:

The B-model is used in the manuscript for fitting data and is governed by Equations 18, 28, and 29 as explained above. The model takes into account the shape of the laminar flow profile, the angle the cell makes against the flow profile, and the arc length of the cell.

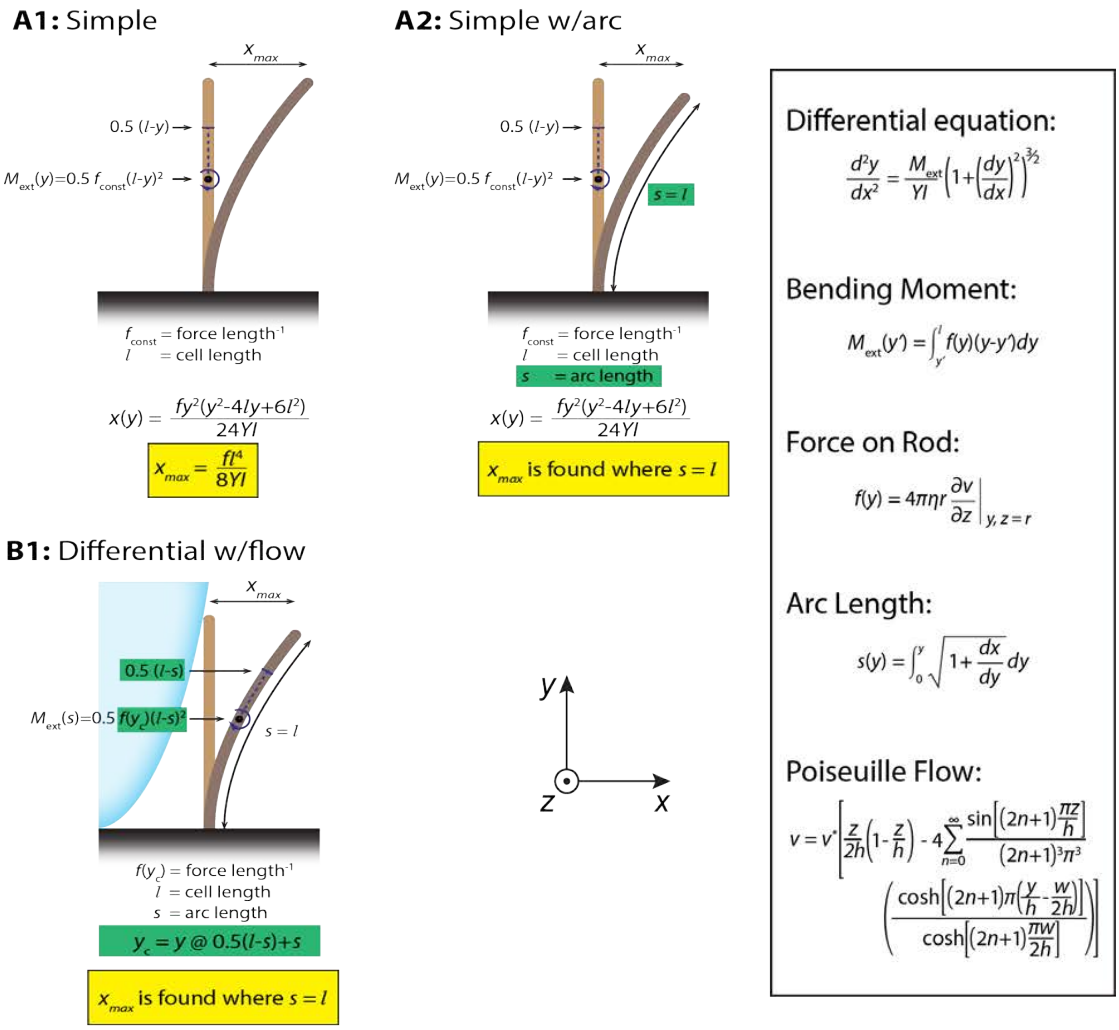


**Figure S18. Schematic of the models described in this section.**

## Practical Considerations for Solving the Numerical Model

To solve a differential equation, we need to set the coordinate space and produce the initial conditions. At first, it would seem prudent to solve the differential equation so that the slope at the origin (base of cell) is zero, as in Figure S15. This strategy works quite well until the cell becomes very long or very flexible. This is a problem because, at large deformations, the slope near the end of the cell could become -∞. Alternatively, rotation of the cell counter-clockwise by 90 degrees creates a problem at the origin (i.e. a slope of +∞). This issue is easily solved by rotating the solution between the two extremes at 45 degrees, giving the initial condition of dy/dx = +1 at the origin and a minimum slope of -1 along the cell. The rotation of the coordinate system does not in any way alter the differential equation (Equation 18), since the curvature is indifferent to orientation. However, the solution must be rotated back into normal space as follows:

$$y = \frac{x_{rot}}{\sqrt{2}} + \frac{y_{rot}}{\sqrt{2}} \quad (33)$$

$$x = \frac{x_{rot}}{\sqrt{2}} - \frac{y_{rot}}{\sqrt{2}} \quad (34)$$

The numerical solution also requires the arc length as a function of $y$. This function, $s(y)$, will change depending on the solution to the differential equation (hence this is an integro-differential equation). Therefore, an iterative process of solving the differential equation then calculating the arc length, putting it back into the differential equation, and so forth is required until a solution has converged. The convergence is determined by minimization of chi-squared, which is defined as:

$$\chi^2 = \sum \frac{(current - prevous)^2}{previous} \quad (35)$$

where a typical desired chi-square value is $1 \times 10^{-20}$ for our system. After convergence, the $x_{max}$ value is calculated by determining the deflection where the cell length, $l$, equals the arc length.

## 5. REFERENCES


1. Tuson HH, Copeland MF, Carey S, Sacotte R, & Weibel DB (2013) Flagellum Density Regulates Proteus mirabilis Swarmer Cell Motility in Viscous Environments. *Journal of Bacteriology* 195(2):368-377.
2. Sliusarenko O, Heinritz J, Emonet T, & Jacobs-Wagner C (2011) High-throughput, subpixel precision analysis of bacterial morphogenesis and intracellular spatio-temporal dynamics. *Mol Microbiol* 80(3):612-627.
3. CLSI (2000) *Methods for Dilution Antimicrobial Susceptibility Tests for Bacteria That Grow Aerobically; Approved Standard* (Clinical and Laboratory Standards Institute, Wayne, PA) Fifth Ed.
4. Tivol WF, Briegel A, & Jensen GJ (2008) An improved cryogen for plunge freezing. *Microsc Microanal* 14(5):375-379.
5. Zheng SQ*, et al.* (2007) UCSF tomography: an integrated software suite for real-time electron microscopic tomographic data collection, alignment, and reconstruction. *J Struct Biol* 157(1):138-147.
6. Kremer JR, Mastronarde DN, & McIntosh JR (1996) Computer visualization of three-dimensional image data using IMOD. *J Struct Biol* 116(1):71-76.
7. Nicastro D*, et al.* (2006) The molecular architecture of axonemes revealed by cryoelectron tomography. *Science* 313(5789):944-948.
8. Collins TJ (2007) ImageJ for microscopy. *Biotechniques* 43(1 Suppl):25-30.
9. Turner RD, Hurd AF, Cadby A, Hobbs JK, & Foster SJ (2013) Cell wall elongation mode in Gram-negative bacteria is determined by peptidoglycan architecture. *Nat Commun* 4.
10. Kuhner D, Stahl M, Demircioglu DD, & Bertsche U (2014) From cells to muropeptide structures in 24 h: peptidoglycan mapping by UPLC-MS. *Sci Rep* 4:7494.
11. Strating H, Vandenende C, & Clarke AJ (2012) Changes in peptidoglycan structure and metabolism during differentiation of Proteus mirabilis into swarmer cells. *Can J Microbiol* 58(10):1183-1194.
12. Glauner B (1988) Separation and Quantification of Muropeptides with High-Performance Liquid-Chromatography. *Anal Biochem* 172(2):451-464.
13. Amir A, Babaeipour F, McIntosh DB, Nelson DR, & Jun S (2014) Bending forces plastically deform growing bacterial cell walls. *Proc Natl Acad Sci U S A* 111(16):5778-5783.
14. Hashmi SM, Loewenberg M, & Dufresne ER (2007) Spatially extended FCS for visualizing and quantifying high-speed multiphase flows in microchannels. *Opt Express* 15(10):6528-6533.